UCLA
UCLA Previously Published Works

Title
Turbulent Rayleigh-Bénard convection in spherical shells

Permalink
https://escholarship.org/uc/item/28x3j00j

Authors
Gastine, T
Wicht, J
Aurnou, JM

Publication Date
2015-08-10

DOI
10.1017/jfm.2015.401

Peer reviewed

eScholarship.org Powered by the California Digital Library
University of California

arXiv:1504.02633v1 [physics.flu-dyn] 10 Apr 2015

Turbulent Rayleigh-Bénard convection in spherical shells

Thomas Gastine[1]†, Johannes Wicht[1], Jonathan M. Aurnou[2]

[1]Max Planck Institut für Sonnensystemforschung, Justus-von-Liebig-Weg 3, 37077 Göttingen, Germany,

[2]Department of Earth, Planetary and Space Sciences, University of California, Los Angeles, CA, 90095-1567 USA

(Received ?; revised ?; accepted ?. - To be entered by editorial office)

We consider numerical models of Boussinesq convection in non-rotating spherical shells for a fluid with a unity Prandtl number and Rayleigh numbers up to 10^9. In this geometry, curvature and radial variations of the gravitationnal acceleration yield asymmetric boundary layers. A systematic parameter study for various radius ratios (from $\eta = r_i/r_o = 0.2$ to $\eta = 0.95$) and gravity profiles allows us to explore the dependence of the asymmetry on these parameters. We find that the average plume spacing is conserved between the spherical inner and outer bounding surfaces. An estimate of the average plume separation allows us to accurately predict the boundary layer asymmetry for the various spherical shell configurations explored here. The mean temperature and horizontal velocity profiles are in good agreement with classical Prandtl-Blasius laminar boundary layer profiles, provided the boundary layers are analysed in a dynamical frame, that fluctuates with the local and instantaneous boundary layer thicknesses. The scaling properties of the Nusselt and Reynolds numbers are investigated by separating the different contributions to the thermal and viscous dissipation rates using numerical models with $\eta = 0.6$ and a gravity proportional to $1/r^2$. We show that our spherical models are consistent with the predictions of Grossmann & Lohse's (2000) theory and that $Nu(Ra)$ and $Re(Ra)$ scalings are in good agreement with plane layer results.

Key words: Bénard convection, boundary layers, geophysical and geological flows

1. Introduction

Thermal convection is ubiquitous in geophysical and astrophysical fluid dynamics and rules, for example, turbulent flows in the interiors of planets and stars. The so-called Rayleigh-Bénard (hereafter RB) convection is probably the simplest paradigm to study heat transport phenomena in these natural systems. In this configuration, convection is driven in a planar fluid layer cooled from above and heated from below (Fig. 1(a)). The fluid is confined between two rigid impenetrable walls maintained at constant temperatures. The key issue in RB convection is to understand the turbulent transport mechanisms of heat and momentum across the layer. In particular, how does the heat transport, characterised by the Nusselt number Nu, and the flow amplitude, characterised by the Reynolds number Re, depend on the various control parameters of the system, namely the Rayleigh number Ra, the Prandtl number Pr and the cartesian aspect ratio Γ? In general, $\Gamma = W/H$ quantifies the fluid layer width W over its height H in classical planar

† Email address for correspondence: gastine@mps.mpg.de

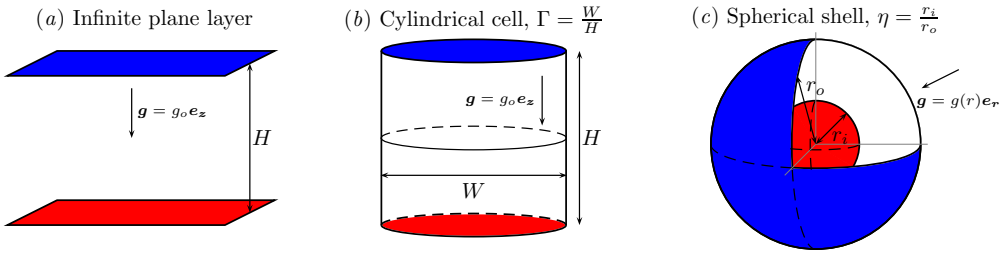

FIGURE 1. Schematic showing different Rayleigh-Bénard convection setups. (a) An infinitely extended fluid layer of height H heated from below and cooled from above. (b) The typical RB convection setup in a cylindrical cell of aspect ratio $\Gamma = W/H$. (c) Convection in a spherical shell with a radius ratio $\eta = r_i/r_o$ with a radially inward gravity. In the three panels, the red and the blue surfaces correspond to the hot and cold boundaries held at constant temperatures.

or cylindrical RB cells. In spherical shells, we rather employ the ratio of the inner to the outer radius $\eta = r_i/r_o$ to characterise the geometry of the fluid layer.

Laboratory experiments of RB convection are classically performed in rectangular or in cylindrical tanks with planar upper and lower bounding surfaces where the temperature contrast is imposed (see Fig. 1(b)). In such a system, the global dynamics are strongly influenced by the flow properties in the thermal and kinematic boundary layers that form in the vicinity of the walls. The characterisation of the structure of these boundary layers is crucial for a better understanding of the transport processes. The marginal stability theory by Malkus (1954) is the earliest boundary layer model and relies on the assumption that the thermal boundary layers adapt their thicknesses to maintain a critical boundary layer Rayleigh number, which implies $Nu \sim Ra^{1/3}$. Assuming that the boundary layers are sheared, Shraiman & Siggia (1990) later derived a theoretical model that yields scalings of the form $Nu \sim Ra^{2/7}\,Pr^{-1/7}$ and $Re \sim Ra^{3/7}\,Pr^{-5/7}$ (see also Siggia 1994). These asymptotic laws were generally consistent with most of the experimental results obtained in the 1990s up to $Ra \lesssim 10^{11}$. Within the typical experimental resolution of one percent, simple power laws of the form $Nu \sim Ra^{\alpha}Pr^{\beta}$ were found to provide an adequate representation with α exponents ranging from 0.28 to 0.31, in relatively good agreement with the Shraiman & Siggia model (e.g. Castaing *et al.* 1989; Chavanne *et al.* 1997; Niemela *et al.* 2000). However, later high-precision experiments by Xu *et al.* (2000) revealed that the dependence of Nu upon Ra cannot be accurately described by such simple power laws. In particular, the local slope of the function $Nu(Ra)$ has been found to increase slowly with Ra. The effective exponent $\alpha_{\rm eff}$ of $Nu \sim Ra^{\alpha_{\rm eff}}$ roughly ranges from values close to 0.28 near $Ra \sim 10^7 - 10^8$ to 0.33 when $Ra \sim 10^{11} - 10^{12}$ (e.g. Funfschilling *et al.* 2005; Cheng *et al.* 2015).

Grossmann & Lohse (2000, 2004) derived a competing theory capable of capturing this complex dynamics (hereafter GL). This scaling theory is built on the assumption of laminar boundary layers of Prandtl-Blasius (PB) type (Prandtl 1905; Blasius 1908). According to the GL theory, the flows are classified in four different regimes in the $Ra-Pr$ phase space according to the relative contribution of the bulk and boundary layer viscous and thermal dissipation rates. The theory predicts non-power-law behaviours for Nu and Ra in good agreement with the dependence $Nu = f(Ra, Pr, \Gamma)$ and $Re = f(Ra, Pr, \Gamma)$ observed in recent experiments and numerical simulations of RB convection in planar or cylindrical geometry (see for recent reviews Ahlers *et al.* 2009; Chillà & Schumacher 2012).

Benefiting from the interplay between experiments and direct numerical simulations

(DNS), turbulent RB convection in planar and cylindrical cells has received a lot of interest in the past two decades. However, the actual geometry of several fundamental astrophysical and geophysical flows is essentially three-dimensional within concentric spherical upper and lower bounding surfaces under the influence of a radial buoyancy force that strongly depends on radius. The direct applicability of the results derived in the planar geometry to spherical shell convection is thus questionable.

As shown in Fig. 1(c), convection in spherical shells mainly differs from the traditional plane layer configuration because of the introduction of curvature and the absence of side walls. These specific features of thermal convection in spherical shells yield significant dynamical differences with plane layers. For instance, the heat flux conservation through spherical surfaces implies that the temperature gradient is larger at the lower boundary than at the upper one to compensate for the smaller area of the bottom surface. This yields a much larger temperature drop at the inner boundary than at the outer one. In addition, this pronounced asymmetry in the temperature profile is accompanied by a difference between the thicknesses of the inner and the outer thermal boundary layers. Following Malkus's marginal stability arguments, Jarvis (1993) and Vangelov & Jarvis (1994) hypothesised that the thermal boundary layers in curvilinear geometries adjust their thickness to maintain the same critical boundary layer Rayleigh number at both boundaries. This criterion is however in poor agreement with the results from numerical models (e.g. Deschamps *et al.* 2010). The exact dependence of the boundary layer asymmetry on the radius ratio and the gravity distribution thus remains an open question in thermal convection in spherical shells (Bercovici *et al.* 1989; Jarvis *et al.* 1995; Sotin & Labrosse 1999; Shahnas *et al.* 2008; O'Farrell *et al.* 2013). This open issue sheds some light on the possible dynamical influence of asymmetries between the hot and cold surfaces that originate due to both the boundary curvature and the radial dependence of buoyancy in spherical shells.

Ground-based laboratory experiments involving spherical geometry and a radial buoyancy forcing are limited by the fact that gravity is vertically downwards instead of radially inwards (Scanlan *et al.* 1970; Feldman & Colonius 2013). A possible way to circumvent this limitation is to conduct experiments under microgravity to suppress the vertically downward buoyancy force. Such an experiment was realised by Hart *et al.* (1986) who designed a hemispherical shell that flew on board of the space shuttle Challenger in May 1985. The radial buoyancy force was modelled by imposing an electric field across the shell. The temperature dependence of the fluid's dielectric properties then produced an effective radial gravity that decreases with the fifth power of the radius (i.e. $g \sim 1/r^5$). More recently, a similar experiment named "GeoFlow" was run on the International Space Station, where much longer flight times are possible (Futterer *et al.* 2010; Futterer *et al.* 2013). This later experiment was designed to mimic the physical conditions in the Earth mantle. It was therefore mainly dedicated to the observation of plume-like structures in a high Prandtl number regime ($Pr > 40$) for $Ra \leq 10^6$. Unfortunately, this limitation to relatively small Rayleigh numbers makes the GeoFlow experiment quite restricted regarding asymptotic scaling behaviours in spherical shells.

To compensate the lack of laboratory experiments, three dimensional numerical models of convection in spherical shells have been developed since the 1980s (e.g. Zebib *et al.* 1980; Bercovici *et al.* 1989, 1992; Jarvis *et al.* 1995; Tilgner 1996; Tilgner & Busse 1997; King *et al.* 2010; Choblet 2012). The vast majority of the numerical models of non-rotating convection in spherical shells has been developed with Earth's mantle in mind. These models therefore assume an infinite Prandtl number and most of them further include a strong dependence of viscosity on temperature to mimic the complex rheology of the mantle. Several recent studies of isoviscous convection with infinite Prandtl number in

spherical shells have nevertheless been dedicated to the analysis of the scaling properties of the Nusselt number. For instance, Deschamps *et al.* (2010) measured convective heat transfer in various radius ratios ranging from $\eta = 0.3$ to $\eta = 0.8$ and reported $Nu \sim Ra^{0.273}$ for $10^4 \leq Ra \leq 10^7$, while Wolstencroft *et al.* (2009) computed numerical models with Earth's mantle geometry ($\eta = 0.55$) up to $Ra = 10^8$ and found $Nu \sim Ra^{0.294}$. These studies also checked the possible influence of internal heating and reported quite similar scalings.

Most of the numerical models of convection in spherical shells have thus focused on the very specific dynamical regime of the infinite Prandtl number. The most recent attempt to derive the scaling properties of Nu and Re in non-rotating spherical shells with finite Prandtl numbers is the study of Tilgner (1996). He studied convection in self-graviting spherical shells (i.e. $g \sim r$) with $\eta = 0.4$ spanning the range $0.06 \leq Pr \leq 10$ and $4 \times 10^3 \leq Ra \leq 8 \times 10^5$. This study was thus restricted to low Rayleigh numbers, relatively close to the onset of convection, which prevents the derivation of asymptotic scalings for $Nu(Ra, Pr)$ and $Re(Ra, Pr)$ in spherical shells.

The objectives of the present work are twofold: (*i*) to study the scaling properties of Nu and Re in spherical shells with finite Prandtl number; (*ii*) to better characterise the inherent asymmetric boundary layers in thermal convection in spherical shells. We therefore conduct two systematic parameter studies of turbulent RB convection in spherical shells with $Pr = 1$ by means of three dimensional DNS. In the first set of models, we vary both the radius ratio (from $\eta = 0.2$ to $\eta = 0.95$) and the radial gravity profile (considering $g(r) \in [r/r_o, 1, (r_o/r)^2, (r_o/r)^5]$) in a moderate parameter regime (i.e. $5 \leq Nu \leq 15$) to study the influence of these properties on the boundary layer asymmetry. We then consider a second set of models with $\eta = 0.6$ and $g \sim 1/r^2$ up to $Ra = 10^9$. These DNS are used to check the applicability of the GL theory to thermal convection in spherical shells. We therefore numerically test the different basic prerequisites of the GL theory: we first analyse the nature of the boundary layers before deriving the individual scaling properties for the different contributions to the viscous and thermal dissipation rates.

The paper is organised as follows. In § 2, we present the governing equations and the numerical models. We then focus on the asymmetry of the thermal boundary layers in § 3. In § 4, we analyse the nature of the boundary layers and show that the boundary layer profiles are in agreement with the Prandtl-Blasius theory (Prandtl 1905; Blasius 1908). In § 5, we investigate the scaling properties of the viscous and thermal dissipation rates before calculating the $Nu(Ra)$ and $Re(Ra)$ scalings in § 6. We conclude with a summary of our findings in § 7.

2. Model formulation

2.1. *Governing hydrodynamical equations*

We consider Rayleigh-Bénard convection of a Boussinesq fluid contained in a spherical shell of outer radius r_o and inner radius r_i. The boundaries are impermeable, no slip and at constant temperatures T_{bot} and T_{top}. We adopt a dimensionless formulation using the shell gap $d = r_o - r_i$ as the reference lengthscale and the viscous dissipation time d^2/ν as the reference timescale. Temperature is given in units of $\Delta T = T_{top} - T_{bot}$, the imposed temperature contrast over the shell. Gravity is non-dimensionalised using its reference value at the outer boundary g_o. The dimensionless equations for the velocity $\boldsymbol{u}$, the pressure p and the temperature T are given by

$$\boldsymbol{\nabla} \cdot \boldsymbol{u} = 0, \tag{2.1}$$

$$\frac{\partial \boldsymbol{u}}{\partial t} + \boldsymbol{u}\cdot\boldsymbol{\nabla}\boldsymbol{u} = -\boldsymbol{\nabla} p + \frac{Ra}{Pr}\, g\, T\, \boldsymbol{e_r} + \boldsymbol{\Delta}\boldsymbol{u}, \tag{2.2}$$

$$\frac{\partial T}{\partial t} + \boldsymbol{u}\cdot\boldsymbol{\nabla} T = \frac{1}{Pr}\Delta T, \tag{2.3}$$

where e_r is the unit vector in the radial direction and g is the gravity. Several gravity profiles have been classically considered to model convection in spherical shells. For instance, self-graviting spherical shells with a constant density correspond to $g \sim r$ (e.g Tilgner 1996), while RB convection models with infinite Prandtl number usually assume a constant gravity in the perspective of modelling Earth's mantle (e.g. Bercovici *et al.* 1989). The assumption of a centrally-condensed mass has also been frequently assumed when modelling rotating convection (e.g. Gilman & Glatzmaier 1981; Jones *et al.* 2011) and yields $g \sim 1/r^2$. Finally, the artificial central force field of the microgravity experiments takes effectively the form of $g \sim 1/r^5$ (Hart *et al.* 1986; Feudel *et al.* 2011; Futterer *et al.* 2013). To explore the possible impact of these various radial distribution of buoyancy on RB convection in spherical shells, we consider different models with the four following gravity profiles: $g \in [r/r_o,\ 1,\ (r_o/r)^2,\ (r_o/r)^5]$. Particular attention will be paid to the cases with $g = (r_o/r)^2$, which is the only radial function compatible with an exact analysis of the dissipation rates (see below, § 2.3).

The dimensionless set of equations (2.1-2.3) is governed by the Rayleigh number Ra, the Prandtl number Pr and the radius ratio of the spherical shell η defined by

$$Ra = \frac{\alpha g_o \Delta T d^3}{\nu\kappa}, \quad Pr = \frac{\nu}{\kappa}, \quad \eta = \frac{r_i}{r_o}, \tag{2.4}$$

where ν and κ are the viscous and thermal diffusivities and α is the thermal expansivity.

2.2. *Diagnostic parameters*

To quantify the impact of the different control parameters on the transport of heat and momentum, we analyse several diagnostic properties. We adopt the following notations regarding different averaging procedures. Overbars $\overline{\cdots}$ correspond to a time average

$$\overline{f} = \frac{1}{\tau}\int_{t_0}^{t_0+\tau} f \,\mathrm{d}t,$$

where τ is the time averaging interval. Spatial averaging over the whole volume of the spherical shell are denoted by triangular brackets $\langle\cdots\rangle$, while $\langle\cdots\rangle_s$ correspond to an average over a spherical surface:

$$\langle f\rangle = \frac{1}{V}\int_V f(r,\theta,\phi)\,\mathrm{d}V; \quad \langle f\rangle_s = \frac{1}{4\pi}\int_0^{\pi}\int_0^{2\pi} f(r,\theta,\phi)\sin\theta\,\mathrm{d}\theta\,\mathrm{d}\phi\,,$$

where V is the volume of the spherical shell, r is the radius, θ the colatitude and ϕ the longitude.

The convective heat transport is characterised by the Nusselt number Nu, the ratio of the total heat flux to the heat carried by conduction. In spherical shells with isothermal boundaries, the conductive temperature profile T_c is the solution of

$$\frac{\mathrm{d}}{\mathrm{d}r}\left(r^2\frac{\mathrm{d}T_c}{\mathrm{d}r}\right) = 0, \quad T_c(r_i) = 1, \quad T_c(r_o) = 0,$$

which yields

$$T_c(r) = \frac{\eta}{(1-\eta)^2}\frac{1}{r} - \frac{\eta}{1-\eta}\,. \tag{2.5}$$

For the sake of clarity, we adopt in the following the notation ϑ for the time-averaged and horizontally-averaged radial temperature profile:

$$\vartheta(r) = \overline{\langle T \rangle_s}\,.$$

The Nusselt number then reads

$$Nu = \frac{\overline{\langle u_r T \rangle_s} - \frac{1}{Pr}\frac{\mathrm{d}\vartheta}{\mathrm{d}r}}{-\frac{1}{Pr}\frac{\mathrm{d}T_c}{\mathrm{d}r}} = -\eta \frac{\mathrm{d}\vartheta}{\mathrm{d}r}(r=r_i) = -\frac{1}{\eta}\frac{\mathrm{d}\vartheta}{\mathrm{d}r}(r=r_o)\,. \tag{2.6}$$

The typical rms flow velocity is given by the Reynolds number

$$Re = \overline{\sqrt{\langle u^2 \rangle}} = \overline{\sqrt{\langle u_r^2 + u_\theta^2 + u_\phi^2 \rangle}}\,, \tag{2.7}$$

while the radial profile for the time and horizontally-averaged horizontal velocity is defined by

$$Re_h(r) = \overline{\left\langle \sqrt{u_\theta^2 + u_\phi^2} \right\rangle_s}\,. \tag{2.8}$$

2.3. *Exact dissipation relationships in spherical shells*

The mean buoyancy power averaged over the whole volume of a spherical shell is expressed by

$$P = \frac{Ra}{Pr}\,\overline{\langle g\, u_r T \rangle} = \frac{4\pi}{V}\,\frac{Ra}{Pr}\int_{r_i}^{r_o} g\, r^2\, \overline{\langle u_r T \rangle_s}\,\mathrm{d}r\,,$$

Using the Nusselt number definition (2.6) and the conductive temperature profile (2.5) then leads to

$$P = \frac{4\pi}{V}\,\frac{Ra}{Pr^2}\left(\int_{r_i}^{r_o} g\, r^2\,\frac{\mathrm{d}\vartheta}{\mathrm{d}r}\,\mathrm{d}r - Nu\,\frac{\eta}{(1-\eta)^2}\int_{r_i}^{r_o} g\,\mathrm{d}r\right)\,.$$

The first term in the parentheses becomes identical to the imposed temperature drop ΔT for a gravity $g \sim 1/r^2$:

$$\int_{r_i}^{r_o} g\, r^2\,\frac{\mathrm{d}\vartheta}{\mathrm{d}r}\,\mathrm{d}r = r_o^2\,[\vartheta(r_o) - \vartheta(r_i)] = -r_o^2\,,$$

and thus yields an analytical relation between P and Nu. For any other gravity model, we have to consider the actual spherically-symmetric radial temperature profile $\vartheta(r)$. Christensen & Aubert (2006) solve this problem by approximating $\vartheta(r)$ by the diffusive solution (2.5) and obtain an approximate relation between P and $\frac{Ra}{Pr^2}(Nu-1)$. This motivates our particular focus on the $g = (r_o/r)^2$ cases which allows us to conduct an exact analysis of the dissipation rates and therefore check the applicability of the GL theory to convection in spherical shells.

Noting that $\frac{\eta}{(1-\eta)^2}\int_{r_i}^{r_o} g\,\mathrm{d}r = -\frac{1}{(1-\eta)^2}$, one finally obtains the exact relation for the viscous dissipation rate ϵ_U:

$$\epsilon_U = \overline{\left\langle (\boldsymbol{\nabla}\times\boldsymbol{u})^2 \right\rangle} = P = \frac{3}{1+\eta+\eta^2}\,\frac{Ra}{Pr^2}\,(Nu-1)\,. \tag{2.9}$$

The thermal dissipation rate can be obtained by multiplying the temperature equation (2.3) by T and integrate it over the whole volume of the spherical shell. This yields

$$\epsilon_T = \overline{\langle (\nabla T)^2 \rangle} = \frac{3\eta}{1+\eta+\eta^2}\,Nu\,. \tag{2.10}$$

These two exact relations (2.9-2.10) can be used to validate the spatial resolutions of the

numerical models with $g = (r_o/r)^2$. To do so, we introduce χ_{ϵ_U} and χ_{ϵ_T}, the ratios of the two sides of Eqs (2.9-2.10):

$$\chi_{\epsilon_U} = \frac{(1+\eta+\eta^2)\,Pr^2}{3\,Ra\,(Nu-1)}\,\epsilon_U\,, \qquad \chi_{\epsilon_T} = \frac{(1+\eta+\eta^2)}{3\eta\,Nu}\,\epsilon_T\,. \tag{2.11}$$

2.4. *Setting up a parameter study*

2.4.1. *Numerical technique*

The numerical simulations have been carried out with the magnetohydrodynamics code MagIC (Wicht 2002). MagIC has been validated via several benchmark tests for convection and dynamo action (Christensen *et al.* 2001; Jones *et al.* 2011). To solve the system of equations (2.1-2.3), the solenoidal velocity field is decomposed into a poloidal and a toroidal contribution

$$\boldsymbol{u} = \boldsymbol{\nabla} \times (\boldsymbol{\nabla} \times W\boldsymbol{e_r}) + \boldsymbol{\nabla} \times Z\boldsymbol{e_r},$$

where W and Z are the poloidal and toroidal potentials. W, Z, p and T are then expanded in spherical harmonic functions up to degree $\ell_{\max}$ in the angular variables θ and ϕ and in Chebyshev polynomials up to degree N_r in the radial direction. The combined equations governing W and p are obtained by taking the radial component and the horizontal part of the divergence of Eq. (2.2). The equation for Z is obtained by taking the radial component of the curl of Eq. (2.2). The equations are time-stepped by advancing the nonlinear terms using an explicit second-order Adams-Bashforth scheme, while the linear terms are time-advanced using an implicit Crank-Nicolson algorithm. At each time step, all the nonlinear products are calculated in the physical space (r, θ, ϕ) and transformed back into the spectral space (r, ℓ, m). For more detailed descriptions of the numerical method and the associated spectral transforms, the reader is referred to (Gilman & Glatzmaier 1981; Tilgner & Busse 1997; Christensen & Wicht 2007).

2.4.2. *Parameter choices*

One of the main focuses of this study is to investigate the global scaling properties of $Pr = 1$ RB convection in spherical shell geometries. This is achieved via measurements of the Nusselt and Reynolds numbers. In particular, we aim to test the applicability of the GL theory to spherical shells. As demonstrated before, only the particular choice of a gravity profile of the form $g \sim 1/r^2$ allows the exactness of the relation Eq. (2.9). Our main set of simulations is thus built assuming $g = (r_o/r)^2$. The radius ratio is kept to $\eta = 0.6$ and the Prandtl number to $Pr = 1$ to allow future comparisons with the rotating convection models by Gastine & Wicht (2012) and Gastine *et al.* (2013) who adopted the same configuration. We consider 35 numerical cases spanning the range $1.5 \times 10^3 \leq Ra \leq 10^9$. Table 1 summarises the main diagnostic quantities for this dataset of numerical simulations and shows that our models basically lie within the ranges $1 < Re < 7000$ and $1 < Nu < 70$.

Another important issue in convection in spherical shells concerns the determination of the average bulk temperature and the possible boundary layer asymmetry between the inner and the outer boundaries (e.g. Jarvis 1993; Tilgner 1996). To better understand the influence of curvature and the radial distribution of buoyancy, we thus compute a second set of numerical models. This additional dataset consists of 113 additional simulations with various radius ratios and gravity profiles, spanning the range $0.2 \leq \eta \leq 0.95$ with

Ra	Nu	Re	λ_T^i/λ_T^o	λ_U^i/λ_U^o	$\epsilon_T^{bu}(\%)$	$\epsilon_U^{bu}(\%)$	χ_{ϵ_T}	χ_{ϵ_U}	$N_r \times \ell_{max}$
1.5×10^3	1.33	4.4	-	-	-	-	1.000	1.000	49×85
2×10^3	1.59	6.7	-	-	-	-	1.000	1.000	49×85
3×10^3	1.80	9.6	-	-	-	-	1.000	1.000	49×85
5×10^3	2.13	14.4	-	-	-	-	1.000	1.000	49×85
7×10^3	2.20	17.5	0.186/0.251	0.076/0.104	0.11	0.57	1.000	1.000	49×85
9×10^3	2.43	21.7	0.168/0.223	0.070/0.094	0.14	0.60	1.000	1.000	49×85
1×10^4	2.51	23.3	0.162/0.217	0.069/0.092	0.15	0.61	1.000	1.000	49×85
1.5×10^4	2.81	29.8	0.143/0.196	0.062/0.086	0.17	0.62	1.000	1.000	49×85
2×10^4	3.05	35.0	0.130/0.185	0.059/0.082	0.15	0.64	1.000	1.000	49×85
3×10^4	3.40	44.0	0.116/0.167	0.054/0.077	0.17	0.64	1.000	1.000	49×85
5×10^4	3.89	57.5	0.102/0.147	0.049/0.069	0.18	0.67	1.000	1.000	49×85
7×10^4	4.27	68.5	0.093/0.133	0.046/0.062	0.18	0.69	1.000	1.000	49×85
1×10^5	4.71	82.3	0.085/0.120	0.043/0.058	0.18	0.70	1.000	1.000	49×85
1.5×10^5	5.28	101.2	0.076/0.107	0.039/0.053	0.19	0.71	1.000	1.000	49×85
2×10^5	5.72	117.0	0.070/0.099	0.037/0.050	0.20	0.74	1.000	1.000	49×85
3×10^5	6.40	143.3	0.062/0.088	0.033/0.046	0.22	0.74	1.000	1.000	61×106
5×10^5	7.37	185.1	0.054/0.077	0.030/0.042	0.24	0.77	1.000	1.000	61×106
7×10^5	8.10	218.6	0.049/0.070	0.028/0.040	0.22	0.77	1.000	1.000	61×106
1×10^6	8.90	259.2	0.045/0.064	0.026/0.037	0.24	0.79	1.000	1.000	81×170
1.5×10^6	9.97	315.1	0.040/0.057	0.024/0.034	0.23	0.81	1.000	1.000	81×170
2×10^6	10.79	362.8	0.037/0.053	0.023/0.032	0.26	0.81	1.000	1.000	81×170
3×10^6	12.11	443.5	0.033/0.048	0.020/0.030	0.24	0.82	0.999	1.003	81×170
5×10^6	13.97	565.6	0.029/0.041	0.018/0.027	0.25	0.83	1.000	1.001	97×266
7×10^6	15.39	666.4	0.026/0.037	0.017/0.025	0.27	0.83	1.000	1.005	97×266
1×10^7	17.07	790.4	0.023/0.034	0.016/0.024	0.25	0.84	1.000	1.005	97×266
1.5×10^7	19.17	960.1	0.021/0.030	0.015/0.021	0.28	0.84	1.000	1.009	97×341
2×10^7	20.87	1099.7	0.019/0.028	0.013/0.020	0.27	0.85	1.000	1.005	121×426
3×10^7	23.50	1335.5	0.017/0.025	0.012/0.018	0.28	0.85	1.000	1.012	121×426
5×10^7	27.35	1690.2	0.014/0.021	0.011/0.016	0.27	0.86	1.000	1.010	161×512
7×10^7	30.21	1999.1	0.013/0.019	0.010/0.015	0.28	0.86	1.000	1.005	201×576
1×10^8	33.54	2329.9	0.012/0.017	0.009/0.013	0.29	0.87	1.000	1.011	201×682
2×10^8	41.49	3239.3	0.010/0.014	0.008/0.012	0.29	0.88	1.000	1.006	321×682
3×10^8	47.22	3882.5	0.008/0.012	0.007/0.010	0.29	0.87	1.001	1.015	321×768
5×10^8	*56.67*	*5040.0*	*0.007/0.009*	*0.005/0.008*	*0.31*	*0.85*	*1.001*	*1.050*	*$321 \times 682^\star$*
5×10^8	55.07	4944.1	0.007/0.011	0.006/0.009	0.29	0.88	0.999	1.003	$401 \times 853^\star$
1×10^9	*73.50*	*7039.4*	*0.005/0.007*	*0.004/0.006*	*0.32*	*0.79*	*1.002*	*1.148*	*$401 \times 682^\star$*
1×10^9	69.01	6836.0	0.006/0.009	0.005/0.007	0.30	0.88	0.999	1.021	$513 \times 1066^\star$

TABLE 1. Summary table of $Pr = 1$ numerical simulations with $\eta = 0.6$ and $g = (r_o/r)^2$. The boundary layer thicknesses and the viscous and thermal dissipations are only given for the cases with $Ra \geq 7 \times 10^3$ when boundary layers can be clearly identified. The italic lines indicate simulations with smaller truncations to highlight the possible resolution problems. The cases with $Ra = 5 \times 10^8$ and $Ra = 10^9$ (highlighted with a star in the last column) have been computed assuming a two-fold symmetry, i.e. effectively simulating only half of the spherical shell in longitude.

$g \in [r/r_o, 1, (r_o/r)^2, (r_o/r)^5]$. To limit the numerical cost of this second dataset, these cases have been mostly run at moderate Rayleigh number and typically span the range $5 < Nu < 15$. Table 2, given in the Appendix, summarises the main diagnostic quantities for this second dataset of numerical simulations.

2.4.3. *Resolution checks*

Attention must be paid to the numerical resolutions of the DNS of RB convection (e.g. Shishkina *et al.* 2010). Especially, underresolving the fine structure of the turbulent flow leads to an overestimate of the Nusselt number, which then falsifies the possible scaling analysis (Amati *et al.* 2005). One of the most reliable ways to validate the truncations employed in our numerical models consists of comparing the obtained viscous and thermal dissipation rates with the average Nusselt number (Stevens *et al.* 2010; Lakkaraju *et al.* 2012; King *et al.* 2012). The ratios χ_{ϵ_U} and χ_{ϵ_T}, defined in Eq. (2.11), are found to be very close to unity for all the cases of Table 1, which supports the adequacy of the employed numerical resolutions. To further highlight the possible impact of inadequate spatial resolutions, two underresolved numerical models for the two highest Rayleigh numbers have also been included in Table 1 (lines in italics). Because of the insufficient number of grid points in the boundary layers, the viscous dissipation rates are significantly higher than expected in the statistically stationary state. This leads to overestimated Nusselt numbers by similar percent differences $(2-10\%)$.

Table 1 shows that the typical resolutions span the range from ($N_r = 49$, $\ell_{\max} = 85$) to ($N_r = 513$, $\ell_{\max} = 1066$). The two highest Rayleigh numbers have been computed assuming a two-fold azimuthal symmetry to ease the numerical computations. A comparison of test runs with or without the two-fold azimuthal symmetry at lower Rayleigh numbers ($5 \times 10^7 \leq Ra \leq 3 \times 10^8$) showed no significant statistical differences. This enforced symmetry is thus not considered to be influential. The total computational time for the two datasets of numerical models represents roughly 5 million Intel Ivy Bridge CPU hours.

3. Asymmetric boundary layers in spherical shells

3.1. *Definitions*

Several different approaches are traditionally considered to define the thermal boundary layer thickness λ_T. They either rely on the horizontally-averaged mean radial temperature profile $\vartheta(r)$ or on the temperature fluctuation σ defined as

$$\sigma = \sqrt{\overline{\left\langle \left(T - \overline{\langle T \rangle_s} \right)^2 \right\rangle}}. \tag{3.1}$$

Among the possible estimates based on $\vartheta(r)$, the slope method (e.g. Verzicco & Camussi 1999; Breuer *et al.* 2004; Liu & Ecke 2011) defines λ_T as the depth where the linear fit to $\vartheta(r)$ near the boundaries intersects the linear fit to the temperature profile at mid-depth. Alternatively, σ exhibits sharp local maxima close to the walls. The radial distance separating those peaks from the corresponding nearest boundary can be used to define the thermal boundary layer thicknesses (e.g. Tilgner 1996; King *et al.* 2013). Figure 2(a) shows that both definitions of λ_T actually yield nearly indistinguishable boundary layer thicknesses. We therefore adopt the slope method to define the thermal boundary layers.

There are also several ways to define the viscous boundary layers. Figure 2(b) shows the vertical profile of the root-mean-square horizontal velocity Re_h. This profile exhibits strong increases close to the boundaries that are accompanied by well-defined peaks. Following Tilgner (1996) and Kerr & Herring (2000), the first way to define the kinematic boundary layer is thus to measure the distance between the walls and these local maxima. This commonly-used definition gives $\lambda^i_{U,m}$ ($\lambda^o_{U,m}$) for the inner (outer) spherical boundary. Another possible method to estimate the viscous boundary layer follows a similar strategy as the slope method that we adopted for the thermal boundary layers (Breuer

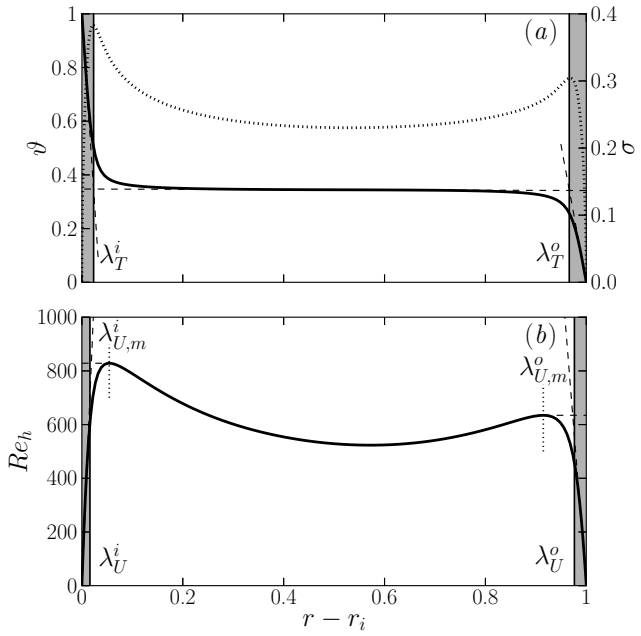

FIGURE 2. (a) Radial profiles of the time and horizontally-averaged mean temperature $\vartheta(r)$ (solid black line) and the temperature variance σ (dotted black line). The thermal boundary layers λ_T^i and λ_T^o are highlighted by the gray shaded area. They are defined as the depths where the linear fit to $\vartheta(r)$ near the top (bottom) crosses the linear fit to the temperature profile at mid-depth (dashed black lines). (b) Radial profiles of the time and horizontally-averaged horizontal velocity $Re_h(r)$. The viscous boundary layers are either defined by the local maxima of Re_h (black dotted lines, $\lambda_{U,m}^i$, $\lambda_{U,m}^o$) or by the intersection of the linear fit to Re_h near the inner (outer) boundary with the tangent to the local maxima (dashed black lines). This second definition is highlighted by a gray shaded area (λ_U^i, λ_U^o). These profiles have been obtained from a numerical model with $Ra = 10^7$, $\eta = 0.6$ and $g = (r_o/r)^2$.

et al. 2004). λ_U^i (λ_U^o) is defined as the distance from the inner (outer) wall where the linear fit to Re_h near the inner (outer) boundary intersects the horizontal line passing through the maximum horizontal velocity.

Figure 2(b) reveals that these two definitions lead to very distinct viscous boundary layer thicknesses. In particular, the definition based on the position of the local maxima of Re_h yields much thicker boundary layers than the tangent intersection method, i.e. $\lambda_{U,m}^{i,o} > \lambda_U^{i,o}$. The discrepancies of these two definitions are further discussed in § 4.

3.2. *Asymmetric thermal boundary layers and mean bulk temperature*

Figure 2 also reveals a pronounced asymmetry in the mean temperature profiles with a much larger temperature drop at the inner boundary than at the outer boundary. As a consequence, the mean temperature of the spherical shell $T_m = \frac{1}{V}\int_V T\,\mathrm{d}V$ is much below $\Delta T/2$. Determining how the mean temperature depends on the radius ratio η has been an ongoing open question in mantle convection studies with infinite Prandtl number (e.g. Bercovici *et al.* 1989; Jarvis 1993; Vangelov & Jarvis 1994; Jarvis *et al.* 1995; Sotin & Labrosse 1999; Shahnas *et al.* 2008; Deschamps *et al.* 2010; O'Farrell *et al.* 2013). To analyse this issue in numerical models with $Pr = 1$, we have performed a systematic parameter study varying both the radius ratio of the spherical shell η and the gravity profile $g(r)$ (see Table 2). Figure 3 shows some selected radial profiles of

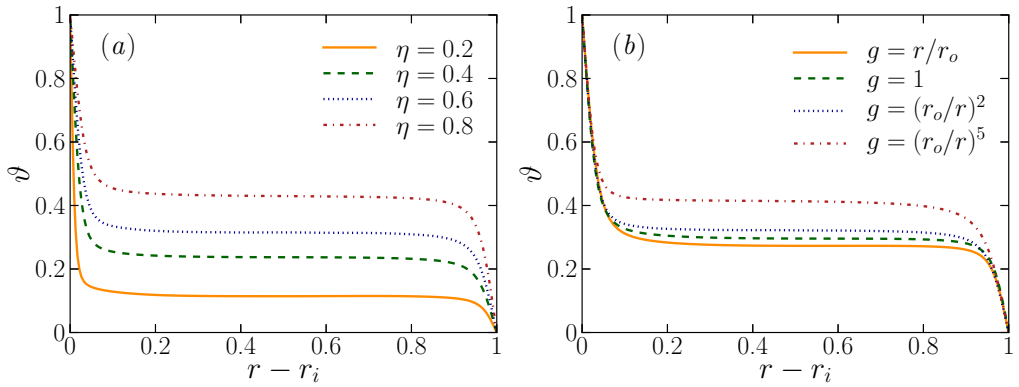

FIGURE 3. (a) $\vartheta(r)$ for different radius ratios η with a gravity $g = (r_o/r)^2$. These models have approximately the same Nusselt number $12 < Nu < 14$. (b) $\vartheta(r)$ for different gravity profiles with a fixed radius ratio $\eta = 0.6$. These models have approximately the same Nusselt number $10 < Nu < 11$.

the mean temperature ϑ for various radius ratios (panel a) and gravity profiles (panel b) for cases with similar Nu. For small values of η, the large difference between the inner and the outer surfaces lead to a strong asymmetry in the temperature distribution: nearly 90% of the total temperature drop occurs at the inner boundary when $\eta = 0.2$. In thinner spherical shells, the mean temperature gradually approaches a more symmetric distribution to finally reach $T_m = 0.5$ when $\eta \to 1$ (no curvature). Figure 3(b) also reveals that a change in the gravity profile has a direct impact on the mean temperature profile. This shows that both the shell geometry and the radial distribution of buoyancy affect the temperature of the fluid bulk in Rayleigh-Bénard convection in spherical shells.

To analytically access the asymmetries in thickness and temperature drop observed in Fig. 3, we first assume that the heat is purely transported by conduction in the thin thermal boundary layers. The heat flux conservation through spherical surfaces (Eq. 2.6) then yields

$$\frac{\Delta T^o}{\lambda_T^o} = \eta^2 \frac{\Delta T^i}{\lambda_T^i}, \tag{3.2}$$

where the thermal boundary layers are assumed to correspond to a linear conduction profile with a temperature drop ΔT^i (ΔT^o) over a thickness λ_T^i (λ_T^o). As shown in Figs. 2-3, the fluid bulk is isothermal and forms the majority of the fluid by volume. We can thus further assume that the temperature drops occur only in the thin boundary layers, which leads to

$$\Delta T^o + \Delta T^i = 1. \tag{3.3}$$

Equations (3.2) and (3.3) are nevertheless not sufficient to determine the three unknowns ΔT^i, ΔT^o, λ_T^o/λ_T^i and an additional physical assumption is required.

A hypothesis frequently used in mantle convection models with infinite Prandtl number in spherical geometry (Jarvis 1993; Vangelov & Jarvis 1994) is to further assume that both thermal boundary layers are marginally stable such that the local boundary layer Rayleigh numbers Ra_λ^i and Ra_λ^o are equal:

$$Ra_\lambda^i = Ra_\lambda^o \;\rightarrow\; \frac{\alpha g_i \Delta T^i {\lambda_T^i}^3}{\nu\kappa} = \frac{\alpha g_o \Delta T^o {\lambda_T^o}^3}{\nu\kappa}. \tag{3.4}$$

This means that both thermal boundary layers adjust their thickness and temperature drop to yield $Ra_\lambda^i \sim Ra_\lambda^o \sim Ra_c \simeq 1000$ (e.g., Malkus 1954). The temperature drops

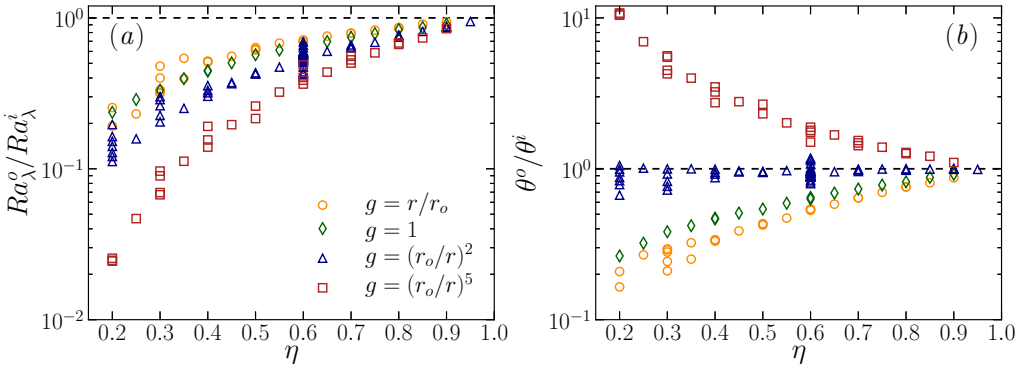

FIGURE 4. (a) Ratio of boundary layer Rayleigh numbers (Eq. 3.4) for various radius ratios and gravity profiles. (b) Ratio of boundary layer temperature scales (Eq. 3.7) for various radius ratios and gravity profiles. The horizontal dashed lines correspond to the hypothetical identity of these properties between both thermal boundary layers, i.e. $Ra^i_\lambda = Ra^o_\lambda$ and $\theta^i = \theta^o$, respectively.

at both boundaries and the ratio of the thermal boundary layer thicknesses can then be derived using Eqs. (3.2-3.3)

$$\Delta T^i = \frac{1}{1+\eta^{3/2}\,\chi_g^{1/4}}, \quad \Delta T^o \simeq T_m = \frac{\eta^{3/2}\,\chi_g^{1/4}}{1+\eta^{3/2}\,\chi_g^{1/4}}, \quad \frac{\lambda^o_T}{\lambda^i_T} = \frac{\chi_g^{1/4}}{\eta^{1/2}}, \tag{3.5}$$

where

$$\chi_g = \frac{g(r_i)}{g(r_o)}, \tag{3.6}$$

is the ratio of the gravitational acceleration between the inner and the outer boundaries. Figure 4(a) reveals that the marginal stability hypothesis is not fulfilled when different radius ratios and gravity profiles are considered. This is particularly obvious for small radius ratios where Ra^o_λ is more than 10 times larger than Ra^i_λ. This discrepancy tends to vanish when $\eta \to 1$, when curvature and gravity variations become unimportant. Deschamps *et al.* (2010) also reported a similar deviation from Eq. (3.5) in their spherical shell models with infinite Prandtl number. They suggest that assuming instead $Ra^o_\lambda/Ra^i_\lambda \sim \eta^2$ might help to improve the agreement with the data. This however cannot account for the additional dependence on the gravity profile visible in Fig. 4(a). We finally note that $Ra_\lambda < 400$ for the database of numerical simulations explored here, which suggests that the thermal boundary layers are stable in all our simulations.

Alternatively Wu & Libchaber (1991) and Zhang *et al.* (1997) proposed that the thermal boundary layers adapt their thicknesses such that the mean hot and cold temperature fluctuations at mid-depth are equal. Their experiments with Helium indeed revealed that the statistical distribution of the temperature at mid-depth was symmetrical. They further assumed that the thermal fluctuations in the center can be identified with the boundary layer temperature scales $\theta^i = \frac{\nu\kappa}{\alpha g_i {\lambda^i_T}^3}$ and $\theta^o = \frac{\nu\kappa}{\alpha g_o {\lambda^o_T}^3}$, which characterise the temperature scale of the thermal boundary layers in a different way than the relative temperature drops ΔT^i and ΔT^o. This second hypothesis yields

$$\theta^i = \theta^o \;\rightarrow\; \frac{\nu\kappa}{\alpha g_i {\lambda^i_T}^3} = \frac{\nu\kappa}{\alpha g_o {\lambda^o_T}^3}, \tag{3.7}$$

and the corresponding temperature drops and boundary layer thicknesses ratio

$$\Delta T^i = \frac{1}{1+\eta^2\,\chi_g^{1/3}}, \quad \Delta T^o = T_m = \frac{\eta^2\,\chi_g^{1/3}}{1+\eta^2\,\chi_g^{1/3}}, \quad \frac{\lambda_T^o}{\lambda_T^i} = \chi_g^{1/3}. \tag{3.8}$$

Figure 4(*b*) shows θ^o/θ^i for different radius ratios and gravity profiles. While all the cases with $g = (r_o/r)^2$ are in relatively good agreement with this predicted scaling, the identity of the boundary layer temperature scales is in general not fulfilled for the other gravity profiles. We note that previous findings by Ahlers *et al.* (2006) already reported that the theory by Wu & Libchaber's does also not hold when the transport properties depend on temperature (i.e. non-Oberbeck-Boussinesq convection).

3.3. *Conservation of the average plume density in spherical shells*

As demonstrated in the previous section, none of the hypotheses classically employed accurately account for the temperature drops and the boundary layer asymmetry observed in spherical shells. We must therefore find a dynamical quantity that can be identified between the two boundary layers.

Figure 5 shows visualisations of the thermal boundary layers for three selected numerical models with different radius ratios and gravity profiles. The isocontours displayed in panels (*a*-*c*) reveal the intricate plume structure. Long and thin sheet-like structures form the main network of plumes. During their migration along the spherical surfaces, these sheet-like plumes can collide and convolute with each other to give rise to mushroom-type plumes (see Zhou & Xia 2010*b*; Chillà & Schumacher 2012). During this morphological evolution, mushroom-type plumes acquire a strong radial vorticity component. These mushroom-type plumes are particularly visible at the connection points of the sheet plumes network at the inner thermal boundary layer (red isosurface in Fig. 5*a*-*c*). Figure 5(*d*-*f*) shows the corresponding equatorial and radial cuts of the temperature fluctuation $T' = T - \vartheta$. These panels further highlight the plume asymmetry between the inner and the outer thermal boundary layers. For instance, the case with $\eta = 0.3$ and $g = (r_o/r)^5$ (top panels) features an outer boundary layer approximately 4.5 times thicker than the inner one. Accordingly, the mushroom-like plumes that depart from the outer boundary layer are significantly thicker than the ones emitted from the inner boundary. This discrepancy tends to vanish in the thin shell case ($\eta = 0.8$, bottom panels) in which curvature and gravity variations play a less significant role ($\lambda_T^o/\lambda_T^i \simeq 1.02$ in that case).

Puthenveettil & Arakeri (2005) and Zhou & Xia (2010*b*) performed statistical analysis of the geometrical properties of thermal plumes in experimental Rayleigh-Bénard convection. By tracking a large number of plumes, their analysis revealed that both the plume separation and the width of the sheet-like plumes follow a log-normal probability density function (PDF). An accurate evaluation of the exact number of plumes for each thermal boundary layer involves a subtle procedure that is very sensitive to the threshold values used to define the plume boundaries.

To further assess how the average plume properties of the inner and outer thermal boundary layers compare with each other in spherical geometry, we adopt a simpler strategy by only focussing on the statistics of the plume density. The plume density per surface unit at a given radius r is expressed by

$$\rho_p \sim \frac{N}{4\pi r^2}, \tag{3.9}$$

where N is the number of plumes, approximated here by the ratio of the spherical surface

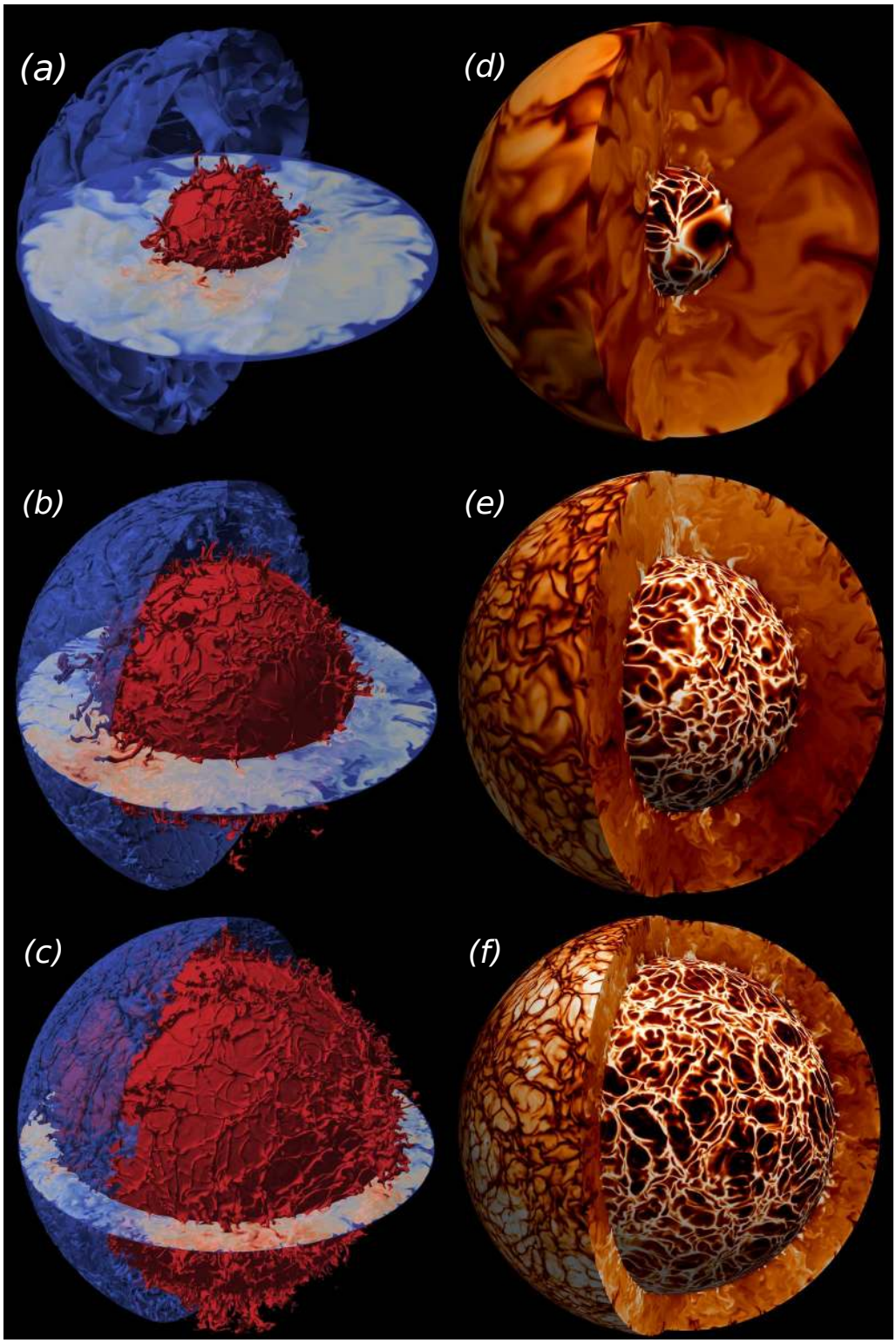

FIGURE 5. (*a-c*) Isosurfaces and equatorial cut of the temperature for three numerical models: hot at the inner thermal boundary layer $T(r = r_i + \lambda_T^i)$ in red, cold at the outer thermal boundary layer $T(r = r_o - \lambda_T^o)$ in blue. (*d-f*) Meridional cuts and surfaces of the temperature fluctuations T'. The inner (outer) surface corresponds to the location of the inner (outer) thermal boundary layers. Color levels range from -0.2 (black) to 0.2 (white). Panels (*a*) and (*d*) correspond to a model with $Ra = 3 \times 10^6$, $\eta = 0.3$ and $g = (r_o/r)^5$. Panels (*b*) and (*e*) correspond to a model with $Ra = 10^8$, $\eta = 0.6$ and $g = (r_o/r)^2$. Panels (*c*) and (*f*) correspond to a model with $Ra = 4 \times 10^7$, $\eta = 0.8$ and $g = r/r_o$.

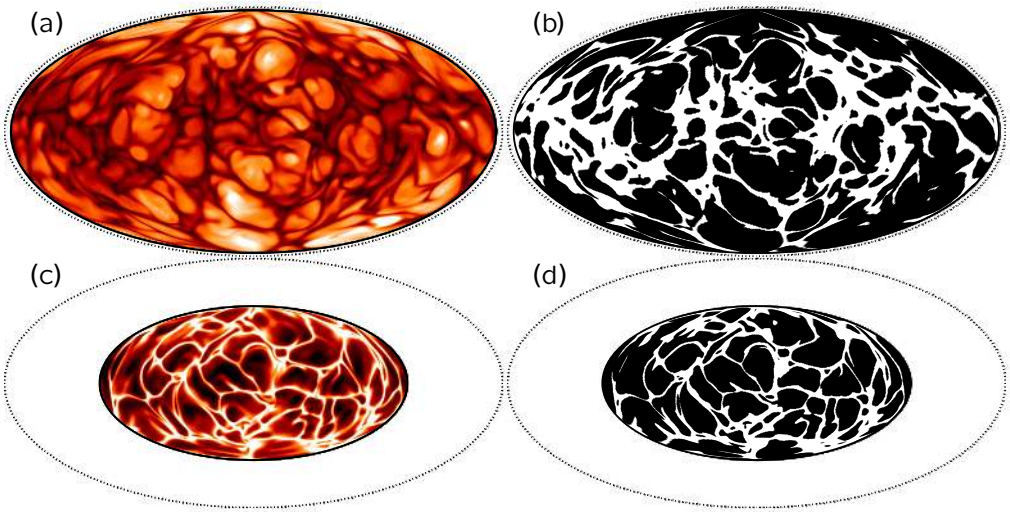

FIGURE 6. (a) Temperature fluctuation at the outer thermal boundary layer $T'(r = r_o - \lambda_T^o)$ displayed in a Hammer projection for a case with $Ra = 10^6$, $\eta = 0.6$, $g = (r_o/r)^2$. (b) Corresponding binarised extraction of the plumes boundaries using Eq. (3.10). (c-d) Corresponding plots at at the inner thermal boundary layer $T'(r = r_i + \lambda_T^i)$. Color levels in panels (a) and (c) range from -0.25 (black) to 0.25 (white). The dotted black line in the four panels correspond to the outer radius of the spherical shell r_o.

to the mean inter-plume area $\bar{\mathcal{S}}$:

$$N \sim \frac{4\pi r^2}{\bar{\mathcal{S}}}.$$

This inter-plume area $\bar{\mathcal{S}}$ can be further related to the average plume separation $\bar{\ell}$ via $\bar{\mathcal{S}} \sim (\pi/4)\,\bar{\ell}^2$. To analyse the statistics of $\mathcal{S}$, we define a given inter-plume area at the inner (outer) thermal boundary layer as an enclosed area surrounded by hot (cold) sheet-like plumes with a thermal perturbation $|T'|$ larger than a threshold $\sigma/2$:

$$\begin{aligned} \mathcal{S}_i(r = r_i + \lambda_T^i) &\equiv \oint_{T'(r_\lambda^i,\theta,\phi)<\sigma(r_\lambda^i)/2} \mathrm{d}\theta\,\mathrm{d}\phi, \\ \mathcal{S}_o(r = r_o - \lambda_T^o) &\equiv \oint_{T'(r_\lambda^o,\theta,\phi)>-\sigma(r_\lambda^o)/2} \mathrm{d}\theta\,\mathrm{d}\phi, \end{aligned} \tag{3.10}$$

The choice of $\sigma/2$ is somewhat arbitrary and can influence the evaluation of the total number of plumes N for each spherical surface. However, the relevant average property $\bar{\mathcal{S}}$, which corresponds to the peak of the PDF, is found to be relatively insensitive to the threshold value.

Figure 6 shows an example of such a characterisation procedure for both thermal boundary layers of a numerical model with $Ra = 10^6$, $\eta = 0.6$, $g = (r_o/r)^2$. The black area in the right panels correspond to the inter-plume spacing defined by Eq. (3.10), while the white area correspond to the complementary plume network location. As expected, the fainter emerging sheet-like plumes are filtered out and only the remaining "skeleton" of the plume network is selected by this extraction process. We then calculate the area of each bounded black surface visible in Fig. 6(b-d) to derive the statistical distribution of the inter-plume area. Figure 7 shows the resulting PDFs obtained by combining several snapshots for the three numerical models of Fig. 5. For the two cases with $\eta = 0.6$ and $\eta = 0.8$ (panels b-c), the statistical distributions for both thermal boundary layers nearly

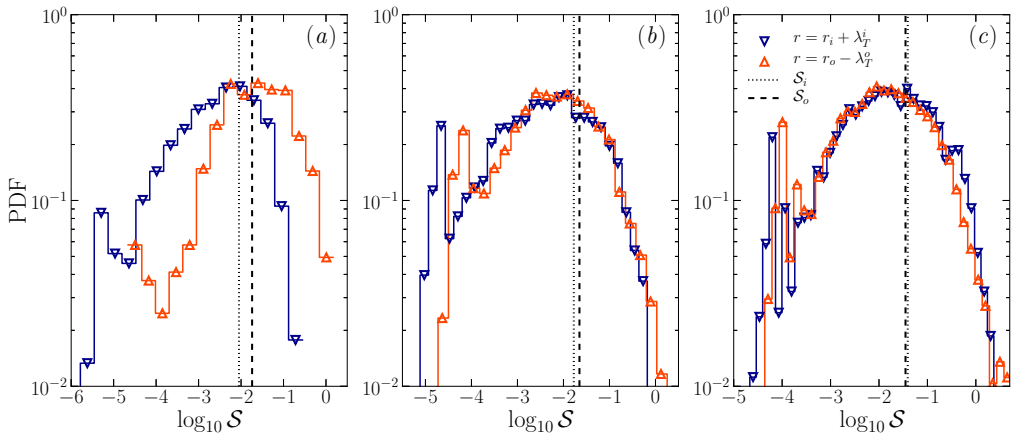

FIGURE 7. Probability density functions (PDFs) of the inter-plume area $\mathcal{S}$ at the outer (orange upward triangles) and at the inner (blue downward triangles) thermal boundary layers for the three numerical models displayed in Fig. 5. The two vertical lines correspond to the predicted values of the mean inter-plume area $\bar{\mathcal{S}}$ derived from Eq. (3.15) for both thermal boundary layers.

overlap. This means that the inter-plume area is similar at both spherical shell surfaces. In contrast, for the case with $\eta = 0.3$ (panel *a*), the two PDFs are slightly offset relative to each other. However, the peak of the distributions remain quite close, meaning that once again the inner and the outer thermal boundary layers share a similar average inter-plume area. Zhou & Xia (2010*b*) demonstrated that the thermal plume statistics in turbulent RB convection follow a log-normal distribution. The large number of plumes in the cases with $\eta = 0.6$ and $\eta = 0.8$ (Fig. 5*b*-*c*) would allow a characterisation of the nature of the statistical distributions. However, this would be more difficult in the $\eta = 0.3$ case (Fig. 5*a*) in which the plume density is significantly weaker. Furthermore, we expect our statistical analysis to become relatively inaccurate when the size of the structures is comparable to the size of the plumes. The secondary humps around $\sim 10^{-5} - 10^{-4}$ visible in Fig. 5 are indeed attributed to this limitation of our characterisation procedure. As a consequence, no further attempt has been made to characterise the exact nature of the PDFs visible in Fig. 7, although the universality of the log-normal statistics reported by Puthenveettil & Arakeri (2005) and Zhou & Xia (2010*b*) likely indicates that the same statistical distribution should hold here too.

The inter-plume area statistics therefore reveals that the inner and the outer thermal boundary layers exhibit a similar average plume density, independently of the spherical shell geometry and the gravity profile. Assuming $\rho_p^o \simeq \rho_p^i$ would allow us to close the system of equations (3.2-3.3) and thus finally estimate ΔT^i, ΔT^o and λ_T^o/λ_T^i. This however requires us to determine an analytical expression of the average inter-plume area $\bar{\mathcal{S}}$ or equivalently of the mean plume separation $\bar{\ell}$ that depends on the boundary layer thickness and the temperature drop. Following Parmentier & Sotin (2000) and King *et al.* (2013), a scaling of $\bar{\ell}$ can be derived from a simple mechanical description of the plume population in each boundary layer. We first hypothesise that the equilibrium number of plumes at the outer/inner boundary layer results from a balance between creation of plumes and disappearance by coalescence with surrounding plumes. The production rate of thermal plumes can be estimated by

$$\mathcal{P} = \frac{N}{\tau_\lambda},$$

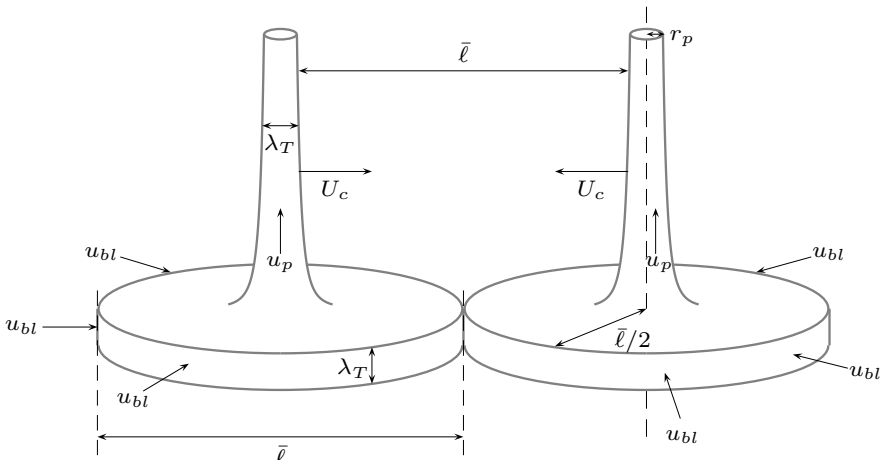

FIGURE 8. Schematic showing two adjacent plumes separated by a distance $\bar{\ell}$. The thermal boundary layer thickness is denoted by λ_T, the plume radius by r_p, the boundary layer flow by u_{bl}, the velocity of migration of the plumes by U_c and the plume velocity by u_p.

where τ_λ is the typical time to produce a new plume. This timescale is approximated by the time to grow a perturbation of the same size as the boundary layer by heat conduction, i.e. $\tau_\lambda \simeq \lambda_T^2/\kappa$. The coalescence rate of plumes is expressed by

$$\mathcal{C} = \frac{N}{\tau_c},$$

where $\tau_c = \bar{\ell}/U_c$ is the typical timescale to coalesce two adjacent plumes separated by a distance $\bar{\ell}$ that approach each other with a velocity U_c. The balance $\mathcal{P} \simeq \mathcal{C}$ for an equilibrated spherical surface then yields an expression of the plume separation $\bar{\ell}$ that depends on U_c

$$\mathcal{P} \simeq \mathcal{C} \quad \rightarrow \quad \bar{\ell} \simeq \frac{U_c\,\lambda_T^2}{\kappa}. \tag{3.11}$$

The schematic diagram in Fig. 8 illustrates the plume separation $\bar{\ell}$ for two plumes that migrate towards each other with a velocity U_c. A second relation comes from the conservation of the volume flow of the boundary layer into a departing plume that can be approximated by

$$2\pi\, u_{bl}\, \frac{\bar{\ell}}{2}\, \lambda_T \simeq \pi\, r_p^2\, u_p\,, \tag{3.12}$$

where u_{bl} is the average boundary layer flow estimated at a distance $\bar{\ell}/2$ from the plume axis; r_p is the radius of a mushroom-type plume and u_p is the radial velocity in a plume. Assuming that the mean plume width scales with the thickness of the thermal boundary layer yields $r_p \simeq \lambda_T/2$. As shown in Fig. 8, the boundary layer flow converges towards two departing plumes that migrate towards each other with a typical velocity U_c. Following Parmentier & Sotin (2000), we simply assume that U_c is comparable to the average boundary layer flow u_{bl}:

$$U_c \simeq u_{bl}\,. \tag{3.13}$$

Finally, the radial velocity in a plume u_p can be inferred by balancing viscosity and buoyancy:

$$\alpha\, g\, \delta T \simeq \nu \frac{u_p}{\lambda_T^2}\,, \tag{3.14}$$

where δT will be replaced by the appropriate temperature drop at the inner (outer) boundary layer ΔT^i (ΔT^o). Combining Eqs. (3.11-3.14) then allows us to eliminate U_c, u_p and u_{bl} and finally provides the following expressions of the average plume separation for both thermal boundary layers:

$$\bar{\ell}_i \simeq \frac{1}{2}\sqrt{\frac{\alpha g_i \Delta T^i {\lambda_T^i}^5}{\nu\kappa}}, \quad \bar{\ell}_o \simeq \frac{1}{2}\sqrt{\frac{\alpha g_o \Delta T^o {\lambda_T^o}^5}{\nu\kappa}}. \tag{3.15}$$

The vertical lines in Fig. 7 correspond to the estimated average inter-plume area for both thermal boundary layers using $\bar{\mathcal{S}}_{i,o} \sim \pi/4\,\bar{\ell}^2_{i,o}$. The predicted average inter-plume area is in good agreement with the peaks of the statistical distributions. Although a more accurate treatment of the plume separation would certainly require further work to disentangle mushroom-shaped thermal plumes and sheet-like structures (Zhou & Xia 2010*b*), the expression (3.15) provides a reasonable estimate of the average plume separation. The identity of the observed plume density at both thermal boundary layers thus yields

$$\rho_p^i = \rho_p^o \;\rightarrow\; \frac{\alpha g_i \Delta T^i {\lambda_T^i}^5}{\nu\kappa} = \frac{\alpha g_o \Delta T^o {\lambda_T^o}^5}{\nu\kappa}. \tag{3.16}$$

Using Eqs. (3.2-3.3) then allows us to finally estimate the temperature jumps and the ratio of the thermal boundary layer thicknesses:

$$\Delta T^i = \frac{1}{1+\eta^{5/3}\,\chi_g^{1/6}}, \quad \Delta T^o = T_m = \frac{\eta^{5/3}\,\chi_g^{1/6}}{1+\eta^{5/3}\,\chi_g^{1/6}}, \quad \frac{\lambda_T^o}{\lambda_T^i} = \frac{\chi_g^{1/6}}{\eta^{1/3}}. \tag{3.17}$$

Figure 9 shows the ratios $\bar{\ell}_o/\bar{\ell}_i$, λ_T^o/λ_T^i and the temperature jumps ΔT^i and ΔT^o. In contrast to the previous criteria, either coming from the marginal stability of the boundary layer (Eq. 3.5, Fig. 4*a*) or from the identity of the temperature fluctuations at mid-shell (Eq. 3.17, Fig. 4*b*), the ratio of the average plume separation $\bar{\ell}_o/\bar{\ell}_i$ now falls much closer to the unity line. Some deviations are nevertheless still visible for spherical shells with $\eta \leq 0.4$ and $g = r/r_o$ (orange circles). The conservation of the plume density between both boundary layers allows us to accurately predict the asymmetry of the thermal boundary layers λ_T^o/λ_T^i and the corresponding temperature drops for the vast majority of the numerical cases explored here (solid lines in panels *b*-*d*).

As we consider a fluid with $Pr = 1$, the viscous boundary layers should show a comparable degree of asymmetry as the thermal boundary layers. Eq. (3.17) thus implies

$$\frac{\lambda_U^o}{\lambda_U^i} = \frac{\lambda_T^o}{\lambda_T^i} = \frac{\chi_g^{1/6}}{\eta^{1/3}}. \tag{3.18}$$

Figure 10 shows the ratio of the viscous boundary layer thicknesses for the different setups explored in this study. The observed asymmetry between the two spherical shell surfaces is in a good agreement with Eq. (3.18) (solid black lines).

3.4. *Thermal boundary layer scalings*

Using Eq. (3.17) and the definition of the Nusselt number (Eq. 2.6), we can derive the following scaling relations for the thermal boundary layer thicknesses:

$$\lambda_T^i = \frac{\eta}{1+\eta^{5/3}\,\chi_g^{1/6}}\,\frac{1}{Nu}, \quad \lambda_T^o = \frac{\eta^{2/3}\chi_g^{1/6}}{1+\eta^{5/3}\,\chi_g^{1/6}}\,\frac{1}{Nu}. \tag{3.19}$$

Figure 11(*a*) demonstrates that the boundary layer thicknesses for the numerical simulations of Table 1 ($g = (r_o/r)^2$ and $\eta = 0.6$) are indeed in close agreement with the

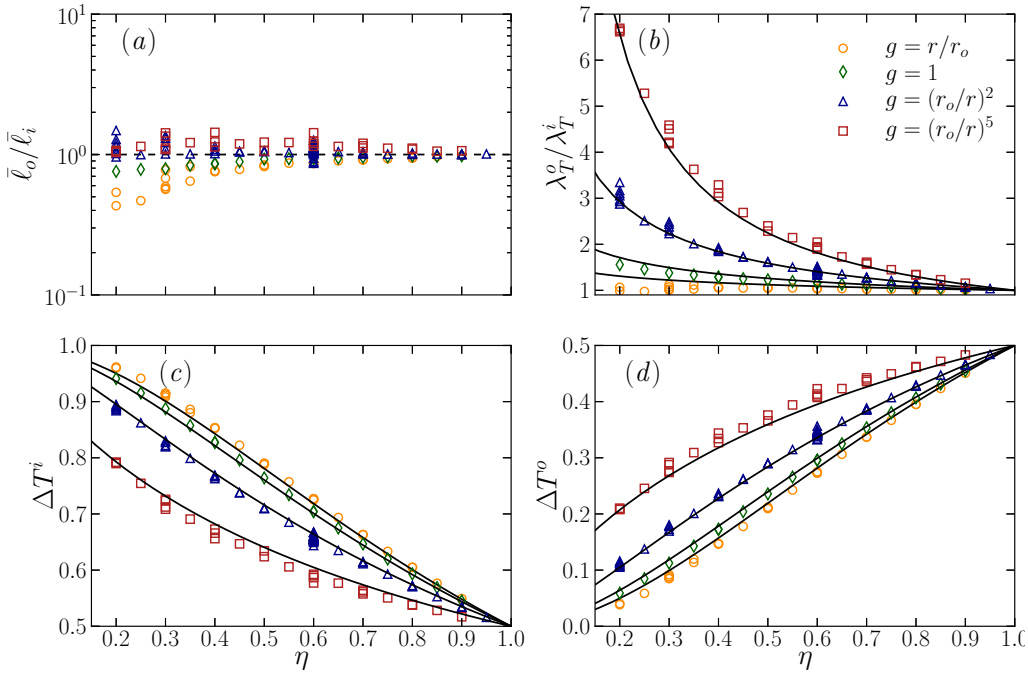

FIGURE 9. (a) Ratio of the thermal plume separation estimated by Eq. (3.15) for various radius ratios and gravity profiles. The horizontal dashed line corresponds to the identity of the average plume separation between both thermal boundary layers, i.e. $\bar{\ell}^i = \bar{\ell}^o$. ($b$) Ratio of thermal boundary layer thicknesses. (c) Temperature drop at the inner boundary layer. (d) Temperature drop at the outer boundary layer. The black lines in panels (b-d) correspond to the theoretical prediction given in Eq. (3.17).

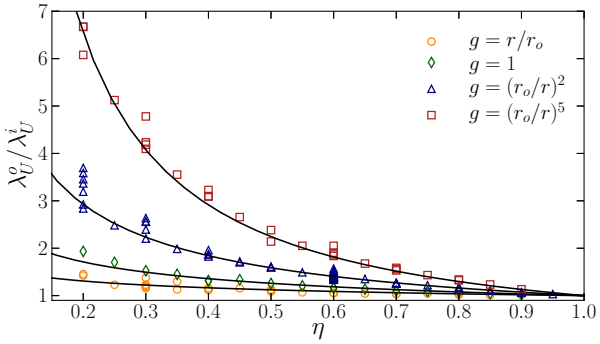

FIGURE 10. Ratio of the viscous boundary layer thicknesses for various aspect ratios and gravity profiles. The black lines correspond to the theoretical prediction given in Eq. (3.18).

theoretical predictions. To further check this scaling for other spherical shell configurations, we introduce the following normalisation of the thermal boundary layer thicknesses

$$\tilde{\lambda}_T^i = \frac{1}{2}\,\frac{1+\eta^{5/3}\,\chi_g^{1/6}}{\eta}\lambda_T^i, \quad \tilde{\lambda}_T^o = \frac{1}{2}\,\frac{1+\eta^{5/3}\,\chi_g^{1/6}}{\eta^{2/3}\,\chi_g^{1/6}}\lambda_T^o.$$

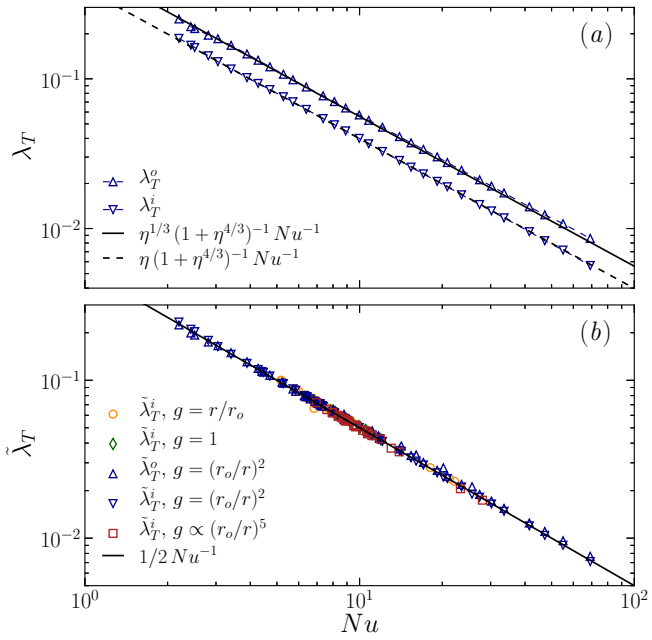

FIGURE 11. (a) Thermal boundary layer thicknesses at the outer boundary (λ_T^i) and at the inner boundary (λ_T^o) as a function of the Nusselt number for the cases of Table 1. The two lines correspond to the theoretical predictions from Eq. (3.19). (b) Normalised boundary layer thicknesses as a function of the Nusselt number for different radius ratios and gravity profiles. For the sake of clarity, the outer boundary layer is only displayed for the cases with $g = (r_o/r)^2$. The solid line corresponds to $\tilde{\lambda}_T = 0.5\,Nu^{-1}$ (Eq. 3.20).

This allows us to derive a unified scaling that does not depend on the choice of the gravity profile or on the spherical shell geometry

$$\tilde{\lambda}_T = \tilde{\lambda}_T^i = \tilde{\lambda}_T^o = \frac{1}{2\,Nu}. \tag{3.20}$$

Figure 11(b) shows this normalised boundary layer thickness for the different spherical shell configurations explored here. Despite the variety of the physical setups, the normalised boundary layer thicknesses are in good agreement with the predicted behaviour.

A closer inspection of Fig. 9(b) and Table 1 however reveals a remaining weak dependence of the ratio λ_T^o/λ_T^i on the Rayleigh number. This is illustrated in Fig. 12 which shows λ_T^o/λ_T^i as a function of Ra for the $\eta = 0.6$, $g = (r_o/r)^2$ cases of Table 1. Although some complex variations are visible, the first-order trend is a very slow increase of λ_T^o/λ_T^i with Ra (10% increase over five decades of Ra). No evidence of saturation is however visible and further deviations from the predicted ratio (horizontal dashed line) might therefore be expected at larger Ra. This variation casts some doubts on the validity of the previous derivation for higher Rayleigh numbers. This may imply that either the plume separation is not conserved at higher Ra; or that the mechanical description of the plume formation is too simplistic to capture the actual plume physics in turbulent convection. Figure 5 for instance shows that the thin sheet-like plumes establish preferred paths for the mushroom-type plume emission. This means that the derivation presented here might miss some ingredients to accurately evaluate the plume spacing and thus characterise the variations in Fig. 12.

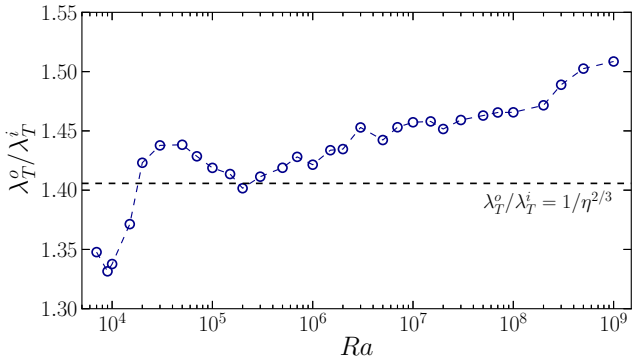

FIGURE 12. Ratio of the thermal boundary layer thicknesses λ_T^o/λ_T^i as a function of the Rayleigh number for the numerical models of Table 1 with $\eta = 0.6$ and $g = (r_o/r)^2$. The horizontal dashed line corresponds to the predicted ratio λ_T^o/λ_T^i given in Eq. (3.17).

4. Boundary layer analysis

The Grossmann Lohse (GL) theory relies on the assumption that the viscous and the thermal boundary layers are not yet turbulent. This is motivated by the observation of small boundary layer Reynolds numbers $Re_s = Re\,\lambda/d < 200$ in experimental convection up to $Ra \simeq 10^{14}$, which remain well below the expected transition to fully turbulent boundary layers (expected at $Re_s \sim 420$, see Ahlers *et al.* 2009). The boundary layer flow is therefore likely laminar and follows the Prandtl-Blasius (PB) laminar boundary layer theory (Prandtl 1905; Blasius 1908; Schlichting & Gersten 2000). The PB theory assumes a balance between the viscous forces, important in the boundary layers, and inertia which dominates in the bulk of the fluid. For the numerical models with unity Prandtl number, this directly implies that the boundary layer thicknesses are inversely proportional to the square-root of Re

$$\lambda_U \sim \lambda_T \sim Re^{-1/2}\,. \tag{4.1}$$

Figure 13(*a*-*b*) shows a test of this theoretical scaling for the two different definitions of the viscous boundary layer introduced in § 3.1. Confirming previous findings by Breuer *et al.* (2004), the commonly-employed definition based on the location of the horizontal velocity maxima yields values that significantly differ from the theoretical prediction (4.1). The least-square fit to the data for the cases with $Re > 250$ indeed gives values relatively close to $\lambda_{U,m} \sim Re^{-1/4}$, an exponent already reported in the experiments by Lam *et al.* (2002) and in the numerical models in cartesian geometry by Breuer *et al.* (2004) and King *et al.* (2013). In addition, $\lambda_{U,m}$ is always significantly larger than λ_T, which is at odds with the expectation $\lambda_T \simeq \lambda_U$ when $Pr = 1$ (see Table 1 for detailed values).

Adopting the intersection of the two tangents to define the viscous boundary layers (Fig. 13*b*) leads to exponents much closer to the predicted value of 1/2 in the high-Re regime. The viscous boundary layer thicknesses obtained with this second definition are in addition found to be relatively close to the thermal boundary layer thicknesses in the high Reynolds regime, i.e. $\lambda_U \simeq \lambda_T$. Therefore, both the expected scaling of λ_U with Re and the similarities between thermal and viscous boundary layer thicknesses strongly suggest that the tangent-intersection method is a more appropriate way to estimate the actual viscous boundary layer. We therefore focus on this definition in the following. For low Reynolds numbers ($Re < 200$), however, the viscous boundary layer thicknesses deviate from the PB theory and follow a shallower slope around $Re^{-0.4}$. This deviation

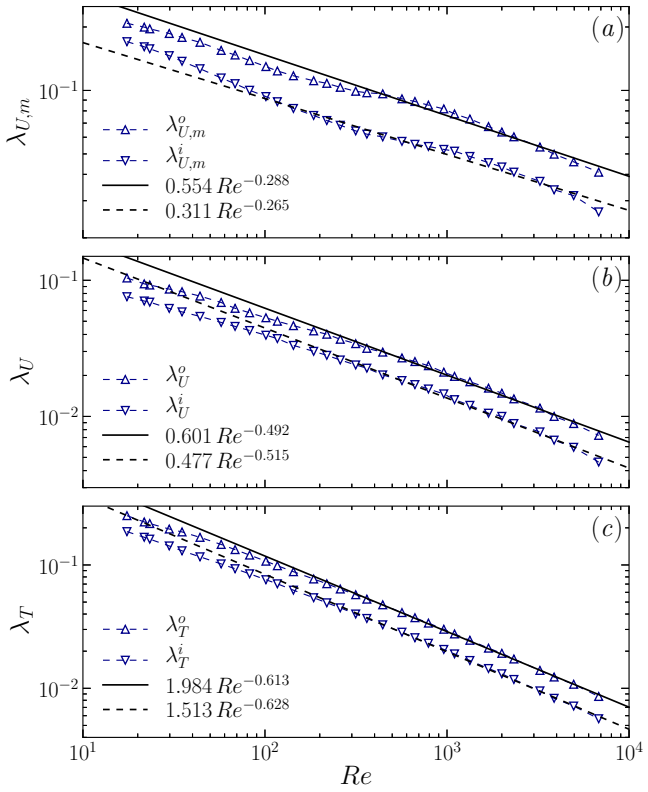

FIGURE 13. (a) Viscous boundary layer thicknesses at the outer boundary ($\lambda^i_{U,m}$) and at the inner boundary ($\lambda^o_{U,m}$) as a function of the Reynolds number for the cases of Table 1 ($\eta = 0.6$, $g = (r_o/r)^2$). (b) Same for the other definition of the viscous boundary layer, i.e. λ^i_U and λ^o_U. (c) Thermal boundary layer thicknesses at the outer boundary (λ^i_T) and at the inner boundary (λ^o_T) as a function of Re. The black lines in panels (a, b and c) correspond to the least-square fit to the data for the numerical models with $Ra \geq 10^6$ (i.e. $Re > 250$).

implies a possible inaccurate description of the low Ra cases by the GL theory (see below).

Figure 13(c) shows that the corresponding scaling of the thermal boundary layer with Re follows a similar trend as the viscous boundary layers. The best fit to the data for the cases with $Re > 250$ yields exponents moderately larger than the theoretical prediction (4.1), while the low$-Re$ cases follow a shallower exponent. At this point, we can simply speculate that this difference might possibly arise because of the inherent dynamical nature of the thermal boundary layers.

For a meaningful comparison with the boundary layer theory, we define new scaling variables for the distance to the spherical shell boundaries. These variables are introduced to compensate for the changes in the boundary layer thicknesses that arise when Ra, η or g are modified. This then allows us to accurately characterise the shape of both the temperature and the flow profiles in the boundary layers and to compare them with the PB boundary layer profiles. To do so, we introduce the self-similarity variables ξ_T and ξ_U for both the inner and the outer spherical shell boundaries:

$$\xi^i_T = \frac{r - r_i}{\lambda^i_T}, \quad \xi^o_T = \frac{r_o - r}{\lambda^o_T}, \quad \xi^i_U = \frac{r - r_i}{\lambda^i_U}, \quad \xi^o_U = \frac{r_o - r}{\lambda^o_U}. \tag{4.2}$$

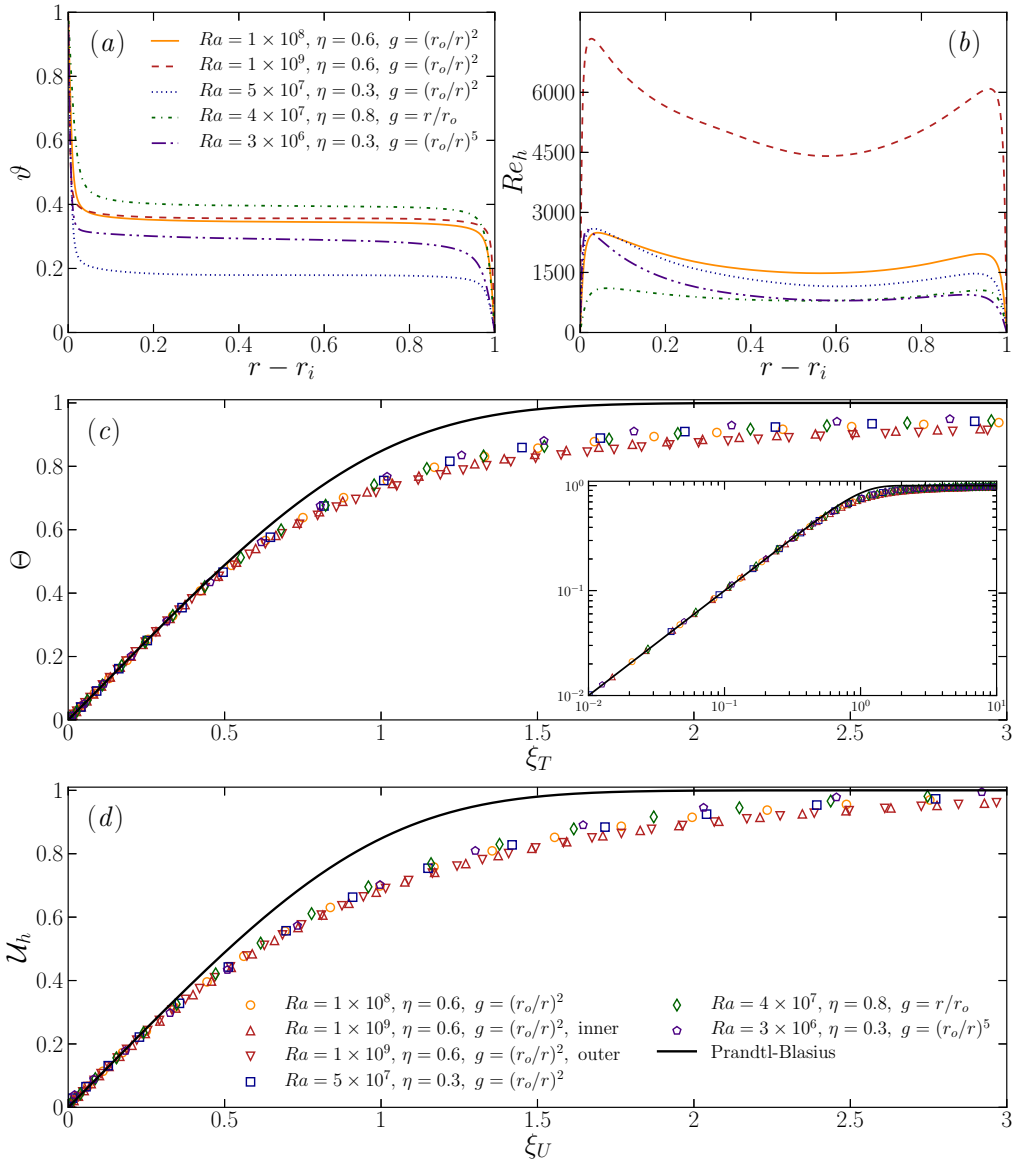

FIGURE 14. (*a-b*) Radial profiles of the time and horizontally-averaged temperature ϑ and horizontal velocity Re_h. (*c*) Θ as a function of ξ_T. (*d*) $\mathcal{U}_h$ as a function of ξ_U. The solid lines in panels (*c-d*) corresponds to the Prandtl-Blasius solution. The inset in panel (*c*) shows Θ in double-logarithmic scale. For the sake of clarity, the outer boundary layer is only displayed for one single case in the panels (*c-d*) ($Ra = 10^9$, $\eta = 0.6$, $g = (r_o/r)^2$).

We accordingly define the following rescaled temperatures for both boundaries

$$\tilde{T}^i(r,\theta,\phi,t) = \frac{T(r,\theta,\phi,t) - \vartheta(r_m)}{T_{bot} - \vartheta(r_m)}, \quad \tilde{T}^o(r,\theta,\phi,t) = \frac{\vartheta(r_m) - T(r,\theta,\phi,t)}{\vartheta(r_m) - T_{top}}, \tag{4.3}$$

where $r_m = (r_i + r_o)/2$ is the mid-shell radius. The rescaled horizontal velocity is simply

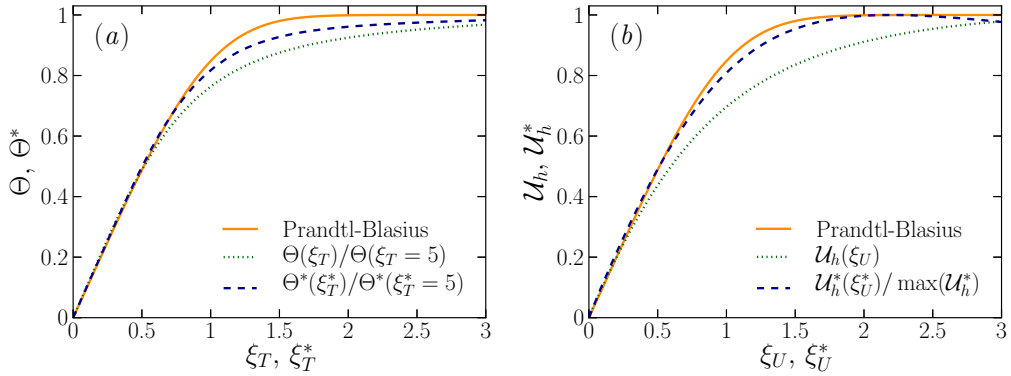

FIGURE 15. (a) Time and horizontally-averaged normalised temperature profile in the fixed reference frame (dotted line, Eq. 4.5) and in the dynamical frame (dashed line, Eq. 4.6) for a case with $Ra = 10^8$, $\eta = 0.6$ and $g = (r_o/r)^2$. (b) Corresponding horizontal velocity profile in the fixed reference frame (dotted line, Eq. 4.5) and in the dynamical frame (dashed line, Eq. 4.7). The solid lines in both panels correspond to the Prandtl-Blasius solution.

obtained by normalisation with its local maximum for each boundary layer:

$$\tilde{u}_h^i(r,\theta,\phi,t) = \frac{u_h(r,\theta,\phi,t)}{\max_i(Re_h)}, \quad \tilde{u}_h^o(r,\theta,\phi,t) = \frac{u_h(r,\theta,\phi,t)}{\max_o(Re_h)}. \tag{4.4}$$

To check the similarity of the profiles, we consider five numerical models with different Ra, η and g. Figure 14(a-b) show the typical mean horizontal velocity and temperature for these cases, while Fig. 14(c-d) show the corresponding time and horizontally-averaged normalised quantities:

$$\Theta = \overline{\left\langle \tilde{T}^{i,o} \right\rangle_s}, \quad \mathcal{U}_h = \overline{\left\langle \tilde{u}_h^{i,o} \right\rangle_s}. \tag{4.5}$$

As already shown in the previous section, the bulk temperature as well as the boundary layer asymmetry strongly depend on the gravity profile and the radius ratio of the spherical shell. Increasing Ra leads to a steepening of the temperature profiles near the boundaries accompanied by a shift of the horizontal velocity maxima towards the walls. Although ϑ and Re_h drastically differ in the five cases considered here, introducing the normalised variables Θ and $\mathcal{U}_h$ allows to merge all the different configurations into one single radial profile. The upward and downward pointing triangles further indicate that those profiles are also independent of the choice of the boundary layer (at the inner or at the outer boundary). Finally, the solutions remain similar to each other when Ra is varied, at least in the interval considered here (i.e. $10^8 \leq Ra \leq 10^9$). These results are in good agreement with the profiles obtained in the numerical simulations by Shishkina & Thess (2009) that cover a similar range of Rayleigh numbers in cylindrical cells with $\Gamma = 1$.

Figure 14(c-d) also compares the numerical profiles with those derived from the PB boundary layer theory. The time-averaged normalised temperature and velocity profiles slightly deviate from the PB profiles, confirming previous 2-D and 3-D numerical models by Zhou & Xia (2010a), Shishkina & Thess (2009) and Stevens *et al.* (2010) This deviation can be attributed to the intermittent nature of plumes that permanently detach from the boundary layers (Sun *et al.* 2008; Zhou & Xia 2010a; du Puits *et al.* 2013). When the boundary layer profiles are obtained from a time-averaging procedure at a fixed height with respect to the container frame (i.e. ξ_T and ξ_U are time-independent), they can actually sample both the bulk and the boundary layer dynamics as the measurement

position can be at time either inside or outside the boundary layer (for instance during a plume emission). To better isolate the boundary layer dynamics, Zhou & Xia (2010*a*) therefore suggested to study the physical properties in a time-dependent frame that accounts for the instantaneous boundary layer fluctuations (see also Zhou *et al.* 2010; Stevens *et al.* 2012).

We apply this dynamical rescaling method to our numerical models by defining local and instantaneous boundary layer thicknesses

$$\xi_T^*(\theta,\phi,t) = \frac{r_o - r}{\lambda_T^o(\theta,\phi,t)}, \quad \xi_U^*(\theta,\phi,t) = \frac{r_o - r}{\lambda_U^o(\theta,\phi,t)}.$$

As the inner and the outer boundary layers exhibit the same behaviour (Fig. 14), we restrict the following discussion to the outer boundary layer. Following Zhou *et al.* (2010) and Shi *et al.* (2012), the horizontal velocity and temperature profiles are given by

$$\mathcal{U}_h^*(\xi_U^*) = \overline{\left\langle \tilde{u}_h\left(r,\theta,\phi,t \,\middle|\, r = r_o - \xi_U^*\lambda_U^o(\theta,\phi,t)\right)\right\rangle_s}, \tag{4.6}$$

$$\Theta^*(\xi_T^*) = \overline{\left\langle \tilde{T}\left(r,\theta,\phi,t \,\middle|\, r = r_o - \xi_T^*\lambda_T^o(\theta,\phi,t)\right)\right\rangle_s}. \tag{4.7}$$

Practically, this dynamical rescaling strategy has been achieved by measuring the local and instantaneous boundary layer for each grid coordinates (θ,ϕ) for several snapshots. Following Zhou & Xia (2010*a*) and Stevens *et al.* (2012), the temperature profiles have been further normalised to some position outside the thermal boundary layer (here $\xi_T = 5$ or $\xi_T^* = 5$) to ease the comparison with the classical definition of the boundary layer in the fixed reference frame (Eq. 4.5). Figure 15 shows an example of this dynamical rescaling method applied to a case with $Ra = 10^8$, $\eta = 0.6$ and $g = (r_o/r)^2$. The temperature and horizontal velocity profiles in the spatially and temporally varying local frame are now in much closer agreement with the PB laminar profiles than those obtained in the fixed reference frame.

Because of the numerical cost of the whole procedure, the dynamical rescaling has only been tested on a limited number of cases. Applying the same method to the numerical model with $Ra = 10^9$ ($\eta = 0.6$, $g = (r_o/r)^2$) yields nearly indistinguishable profiles from those displayed in Fig. 15. This further indicates that boundary layers in spherical shells are laminar in the Ra range explored here and can be well described by the PB theory, provided boundary layers are analysed in a time-dependent frame, which fluctuates with the local and instantaneous boundary layer thicknesses.

5. Dissipation analysis

5.1. *Bulk and boundary layer contributions to viscous and thermal dissipation rates*

The prerequisite of a laminar boundary layer seems fulfilled in our numerical models and we can thus try to apply the GL formalism to our dataset. The idea of the GL theory is to separate the viscous and thermal dissipation rates into two contributions, one coming from the fluid bulk (indicated by the superscript *bu* in the following) and one coming from the boundary layers (*bl*), such that

$$\epsilon_T = \epsilon_T^{bu} + \epsilon_T^{bl}, \quad \epsilon_U = \epsilon_U^{bu} + \epsilon_U^{bl}, \tag{5.1}$$

where the contributions from the bulk are defined by

$$\epsilon_T^{bu} = \frac{4\pi}{V}\int_{r_i+\lambda_T^i}^{r_o-\lambda_T^o} \overline{\left\langle (\nabla T)^2 \right\rangle_s} r^2 \mathrm{d}r, \quad \epsilon_U^{bu} = \frac{4\pi}{V}\int_{r_i+\lambda_U^i}^{r_o-\lambda_U^o} \overline{\left\langle (\boldsymbol{\nabla}\times\boldsymbol{u})^2 \right\rangle_s} r^2 \mathrm{d}r,$$

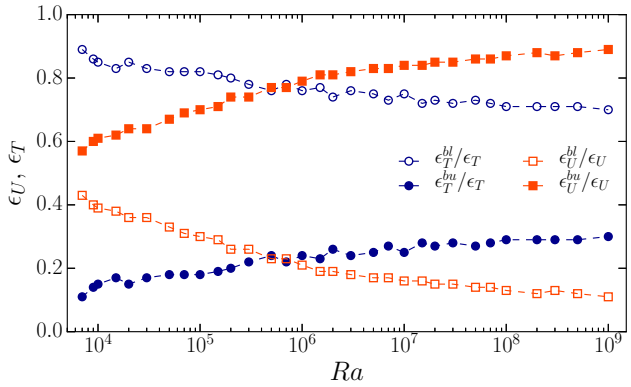

FIGURE 16. Measured contributions of the boundary layer (open symbols) and the fluid bulk (filled symbols) to the total viscous dissipation rate ϵ_U (orange squares) and the total thermal dissipation rate ϵ_T (blue circles).

and the boundary layer contributions are given by

$$\epsilon_T^{bl} = \frac{4\pi}{V}\int_{r_i}^{r_i+\lambda_T^i} \overline{\left\langle (\nabla T)^2 \right\rangle_s}\, r^2 \mathrm{d}r + \frac{4\pi}{V}\int_{r_o-\lambda_T^o}^{r_o} \overline{\left\langle (\nabla T)^2 \right\rangle_s}\, r^2 \mathrm{d}r\,,$$

$$\epsilon_U^{bl} = \frac{4\pi}{V}\int_{r_i}^{r_i+\lambda_U^i} \overline{\left\langle (\boldsymbol{\nabla}\times\boldsymbol{u})^2 \right\rangle_s}\, r^2 \mathrm{d}r + \frac{4\pi}{V}\int_{r_o-\lambda_U^o}^{r_o} \overline{\left\langle (\boldsymbol{\nabla}\times\boldsymbol{u})^2 \right\rangle_s}\, r^2 \mathrm{d}r\,.$$

The RB flows are then classified in the $Ra - Pr$ parameter space according to the dominant contributions to the viscous and thermal dissipation rates. This defines four regimes depending on Ra and Pr: regime I when $\epsilon_U \simeq \epsilon_U^{bl}$ and $\epsilon_T \simeq \epsilon_T^{bl}$; regime II when $\epsilon_U \simeq \epsilon_U^{bu}$ and $\epsilon_T \simeq \epsilon_T^{bl}$; regime III when $\epsilon_U \simeq \epsilon_U^{bl}$ and $\epsilon_T \simeq \epsilon_T^{bu}$; and finally regime IV when $\epsilon_U \simeq \epsilon_U^{bu}$ and $\epsilon_T \simeq \epsilon_T^{bu}$.

For a unity Prandtl number, the GL theory predicts that the flows should be dominated by dissipations in the boundary layer regions at low Ra (regime I). A transition to another regime where dissipations in the fluid bulk dominate (regime IV) is expected to happen roughly around $Ra \simeq 10^8 - 10^{10}$ (Grossmann & Lohse 2000; Ahlers *et al.* 2009; Stevens *et al.* 2013).

Figure 16 shows the relative contributions of the bulk and boundary layers to the viscous and thermal dissipation rates. The viscous dissipation ϵ_U is always dominated by the bulk contribution: starting from roughly 60% at $Ra = 10^4$, it nearly reaches 90% at $Ra = 10^9$. In contrast, the thermal dissipation rate is always dominated by the boundary layer regions, such that ϵ_T^{bu} slowly increases from 10% at $Ra = 10^4$ to 30% at $Ra = 10^9$. According to the GL classification, all our numerical simulations thus belong to the regime II of the $Ra - Pr$ parameter space, in which $\epsilon_U^{bu} > \epsilon_U^{bl}$ and $\epsilon_T^{bl} > \epsilon_T^{bu}$. This seems at odds with the GL theory, which predicts that our DNS should be located either in the regime I or in the regime IV of the parameter space for the range of Ra explored here ($10^3 \leq Ra \leq 10^9$).

The dominance of the boundary layer contribution in the thermal dissipation rate was already reported by Verzicco (2003) for the same range of Ra values. This phenomenon may be attributed to the dynamical nature of the plumes which permanently detach from the boundary layers and penetrate in the bulk of the fluid. These thermal plumes have the same typical size as the boundary layer thickness (Fig. 8) and can thus be thought as "detached boundary layers". Grossmann & Lohse (2004) have therefore suggested to modify their scaling theory to incorporate these detached boundary layers in the thermal

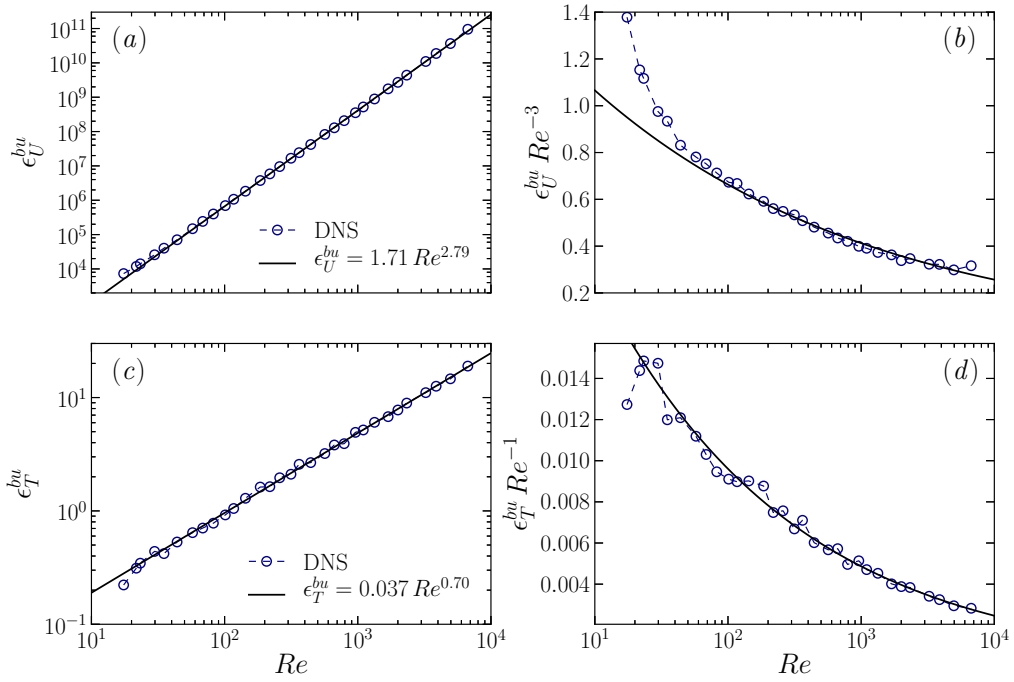

FIGURE 17. (*a*) Viscous dissipation in the bulk of the fluid as a function of Re. (*b*) Corresponding compensated ϵ_U^{bu} scaling. (*c*) Thermal dissipation in the bulk of the fluid as a function of Re. (*d*) Corresponding compensated ϵ_T^{bu} scaling. The solid black lines in the four panels correspond to the least-square fit to the data for the numerical models with $Ra \geq 10^5$.

dissipation rate. They propose to decompose ϵ_T into one contribution coming from the plumes (ϵ_T^{pl}) and one coming from the turbulent background (ϵ_T^{bg})

$$\epsilon_T = \epsilon_T^{pl} + \epsilon_T^{bg}, \tag{5.2}$$

Such a decomposition is however extremely difficult to conduct in spherical shells in which the very large aspect ratio of the convective layer yields a complex and time-dependent multi-cellular large scale circulation (LSC) pattern (see for instance Bailon-Cuba *et al.* 2010, for the influence of large Γ on the LSC). In the following, we therefore first keep the initial decomposition (5.1) before coming back to the inherent problem of accurately separating the different contributions to the dissipation rate in § 5.3.

5.2. *Individual scaling laws for the dissipation rates*

Based on the hypothesis of homogeneous and isotropic turbulence, the GL theory assumes that the thermal and viscous dissipation rates in the bulk of the fluid scale like

$$\epsilon_U^{bu} \sim Re^3, \quad \epsilon_T^{bu} \sim Re, \tag{5.3}$$

in our dimensionless units. Figure 17 shows the bulk dissipation rates as a function of Re for the numerical models of Table 1. The best fit to the data (solid lines) for the cases with $Ra \geq 10^5$ yields $\epsilon_U^{bu} \sim Re^{2.79}$ and $\epsilon_T^{bu} \sim Re^{0.7}$, only roughly similar to the prediction (5.3). These deviations from the theoretical exponents are further confirmed by the compensated scalings $\epsilon_U^{bu}\,Re^{-3}$ and $\epsilon_T^{bu}\,Re^{-1}$ shown in panels (*b*) and (*d*), which show a coherent remaining dependence on Re. Even at high Reynolds numbers, there is no evidence of convergence towards the exact expected scalings from the GL theory. This

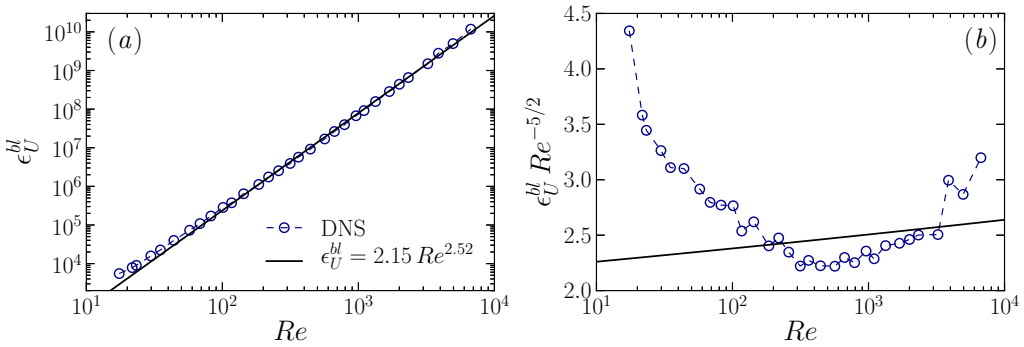

FIGURE 18. (a) Viscous dissipation in the boundary layers as a function of Re. (b) Corresponding compensated ϵ_U^{bl} scaling. The solid black lines in the four panels correspond to the least-square fit to the data for the numerical models with $Ra \geq 10^5$.

is particularly obvious for ϵ_T^{bu} which remains in close agreement with $\epsilon_T^{bu} \sim Re^{0.7}$ for the whole range of Re values explored here (solid line in Fig. 17d). The dependence of ϵ_U^{bu} on Re shows a gradual steepening of the slope when Re increases, which implies that $\epsilon_U^{bu}(Re)$ cannot be accurately represented by a simple power law. Similar deviations from (5.3) have already been reported in the Taylor-Couette flow experiments by Lathrop *et al.* (1992) and in the numerical simulations of RB homogeneous turbulence by Calzavarini *et al.* (2005).

A similar procedure can be applied to the dissipation rates in the boundary layers. In spherical shells, the volume fraction occupied by the boundary layers can be approximated by the following Taylor expansion to the first order

$$f_V(\lambda) = \frac{4\pi}{V}\left(\int_{r_i}^{r_i+\lambda^i} r^2 \mathrm{d}r + \int_{r_o-\lambda^o}^{r_o} r^2 \mathrm{d}r\right) \simeq 3\,\frac{\lambda^i\eta^2 + \lambda^o}{1+\eta+\eta^2},$$

in the limit of thin boundary layers $\lambda \ll r_o - r_i$. The viscous dissipation rate in the boundary layers can then be estimated by

$$\epsilon_U^{bl} \sim \frac{U_{rms}^2}{\lambda_U^2}\, f_V(\lambda_U) \sim \frac{Re^2}{\lambda_U},$$

in our dimensionless units. As demonstrated in § 4, the boundary layers are laminar and are in reasonable agreement with the PB boundary layer theory. This implies that $\lambda_U \sim Re^{-1/2}$ and thus yields

$$\epsilon_U^{bl} \sim Re^{5/2}. \tag{5.4}$$

Figure 18 shows the viscous dissipation rate in the boundary layers as a function of Re for the numerical models of Table 1. The least-square fit to the data (solid lines) yields $\epsilon_U^{bl} \sim Re^{2.52}$, in close agreement with the expected theoretical exponent. The compensated scaling displayed in panel (b) reveals a remaining weak secondary dependence of ϵ_U^{bl} on Re, which is not accurately captured by the power law. The local slope of $\epsilon_U^{bl}(Re)$ initially decreases with Re (when $Re \lesssim 200$) before slowly increasing at higher Reynolds numbers ($Re \gtrsim 200$). This behaviour suggests that, although simple power laws are at first glance in very good agreement with the GL theory, they may not account for the detailed variations of $\epsilon_U^{bl}(Re)$.

The boundary layer contribution to the thermal dissipation rate is estimated in a

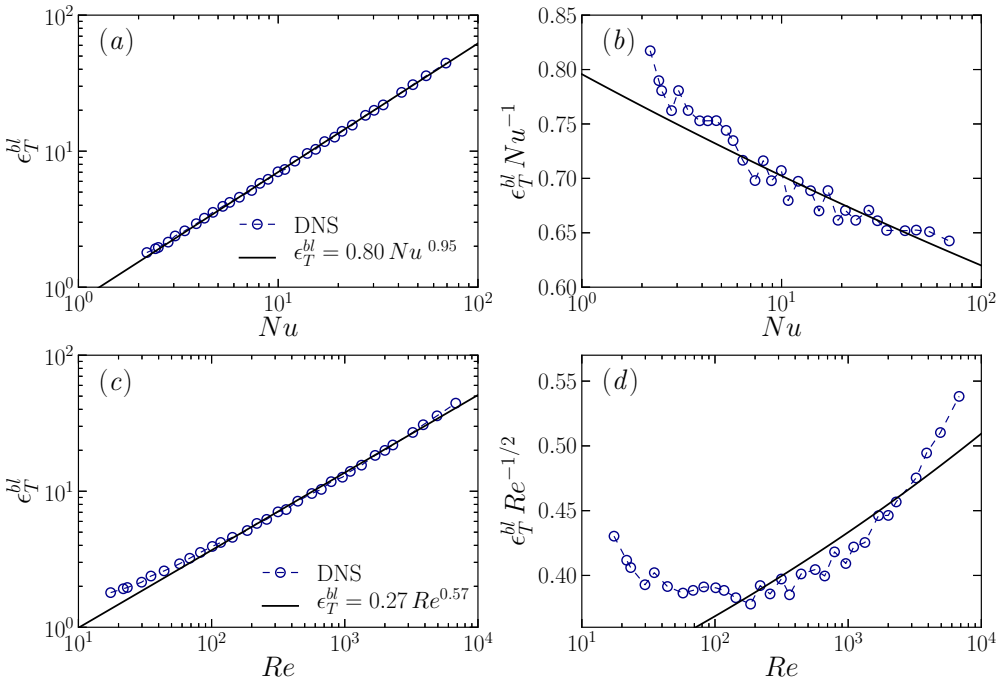

FIGURE 19. (a) Thermal dissipation in the boundary layers as a function of Nu. (b) Corresponding compensated ϵ_T^{bl} scaling. (c) Thermal dissipation in the boundary layers as a function of Re. (d) Corresponding compensated ϵ_T^{bl} scaling. The solid black lines in the four panels correspond to the least-square fit to the data for the numerical models with $Ra \geq 10^5$.

similar way:

$$\epsilon_T^{bl} \sim \frac{\Delta T^2}{\lambda_T^2} f_V(\lambda_T) \sim \frac{1}{\lambda_T},$$

which yields

$$\epsilon_T^{bl} \sim Nu. \tag{5.5}$$

The laminar nature of the boundary layers also implies $\lambda_T \sim Re^{-1/2}$ and thus

$$\epsilon_T^{bl} \sim Re^{1/2}. \tag{5.6}$$

Figure 19 shows ϵ_T^{bl} as a function of Nu and Re for the cases of Table 1. The least-square fits yield $\epsilon_T^{bl} \sim Nu^{0.95}$ and $\epsilon_T^{bl} \sim Re^{0.57}$ (solid lines), close to the expected exponents. However, the compensated scalings displayed in panels (b) and (d) reveal that the linear fit to $\epsilon_T^{bl}(Nu)$ remains in good agreement with the data, while $\epsilon_T^{bl}(Re)$ is not accurately described by such a simple fit. The solutions increasingly deviate from the power law at high Reynolds numbers with the local slope of $\epsilon_T^{bl}(Re)$ that gradually steepens with Re.

5.3. *Individual versus global scalings*

Despite the overall fair agreement with the GL predictions, a close inspection of the dependence of the four dissipation rates on the Reynolds number reveals some remaining dependence on Re, which cannot be perfectly described by simple power laws. This is particularly obvious in the boundary layer contributions $\epsilon_U^{bl}(Re)$ and $\epsilon_T^{bl}(Re)$. In addition, both thermal dissipation rates deviate stronger from the theoretical exponents than their viscous counterparts (see also Verzicco 2003). One obvious problem is the inherent dif-

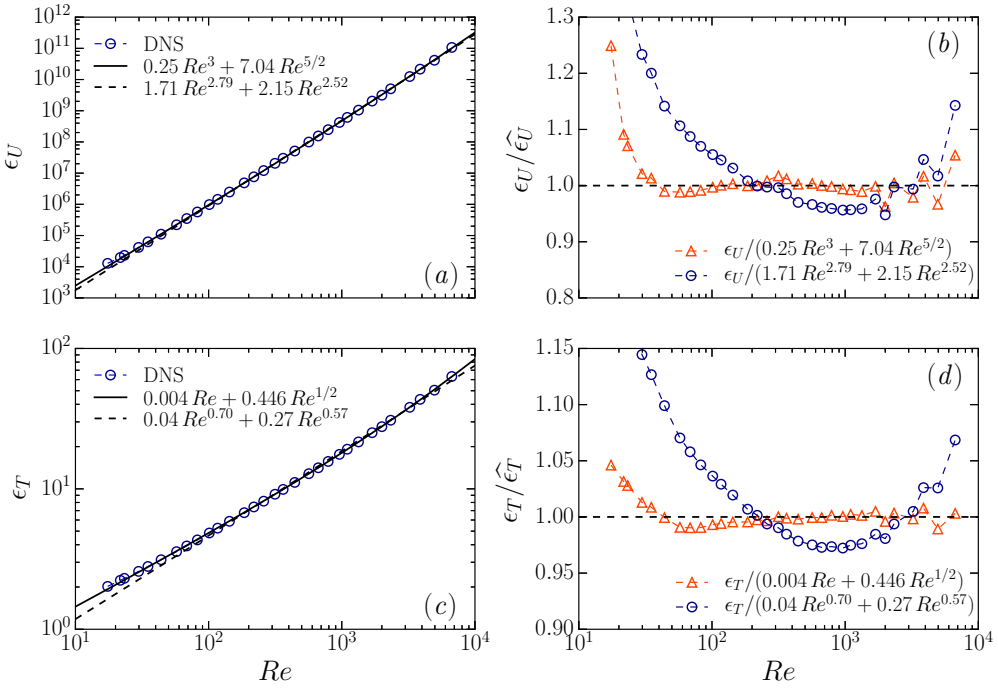

FIGURE 20. (*a*) ϵ_U as a function of Re. (*b*) ϵ_U normalised by the predictions coming from Eq.(5.7) (orange triangles) and Eq. (5.8) (blue circles) as a function of Re. (*c*) ϵ_T as a function of Re. (*d*) ϵ_T normalised by the predictions coming from Eq.(5.7) (orange triangles) and Eq. (5.8) (blue circles) as a function of Re. The dashed black lines in panels (*c*-*d*) correspond to the equality between the asymptotic scalings and the data.

ficult separation of bulk and boundary layer contributions already discussed above. The dynamical plumes constantly departing from the boundary layers obviously complicate matters. To check whether the general idea of a boundary layer and a bulk contribution that both scale with the predicted exponents is at least compatible with the *total* dissipation rates, we directly fit

$$\widehat{\epsilon_U} = \widehat{\epsilon_U^{bu}} + \widehat{\epsilon_U^{bl}} = \quad a\,Re^3 + b\,Re^{5/2}\,,$$
$$\widehat{\epsilon_T} = \widehat{\epsilon_T^{bu}} + \widehat{\epsilon_T^{bl}} = \quad c\,Re + d\,Re^{1/2}\,.$$

This leaves only the four prefactors (a, b, c, d) as free fitting parameters and yields

$$\begin{aligned}\widehat{\epsilon_U} = \widehat{\epsilon_U^{bu}} + \widehat{\epsilon_U^{bl}} = &\quad 0.251\,Re^3 + 7.038\,Re^{5/2}\,,\\ \widehat{\epsilon_T} = \widehat{\epsilon_T^{bu}} + \widehat{\epsilon_T^{bl}} = &\quad 0.004\,Re + 0.446\,Re^{1/2}\,.\end{aligned} \tag{5.7}$$

We then compare this direct least-square fit of the total dissipation rates to the sum of the individual scalings obtained in the previous section

$$\begin{aligned}\widehat{\epsilon_U} = \widehat{\epsilon_U^{bu}} + \widehat{\epsilon_U^{bl}} = &\quad 1.713\,Re^{2.79} + 2.147\,Re^{2.52}\,,\\ \widehat{\epsilon_T} = \widehat{\epsilon_T^{bu}} + \widehat{\epsilon_T^{bl}} = &\quad 0.037\,Re^{0.7} + 0.267\,Re^{0.57}\,.\end{aligned} \tag{5.8}$$

The accuracy of the two scalings (5.7) and (5.8) are compared in Fig. 20, which shows the total viscous and thermal dissipation rates as a function of Re for the numerical models of Table 1. While the two scalings are nearly indistinguishable on the left panels

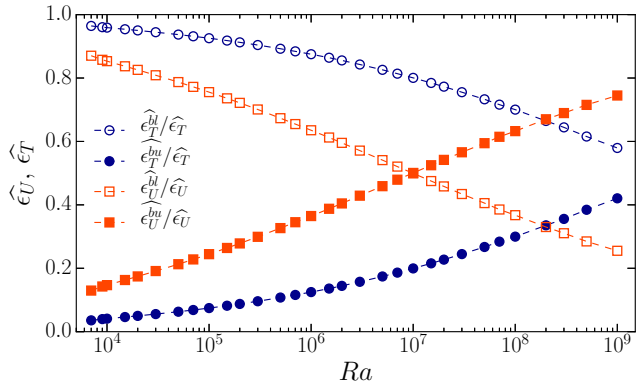

FIGURE 21. Estimated relative contributions of the boundary layer (open symbols) and the fluid bulk (filled symbols) to $\widehat{\epsilon_U}$ (orange squares) and $\widehat{\epsilon_T}$ (blue circles) using Eq. (5.7).

(a) and (c), the corresponding normalised scalings shown in panels (b) and (d) reveal some important differences. The scalings based on the sum of the power laws derived in the last section (Eq. 5.8) are in relatively poor agreement with the data ($5-10\%$ error for $Re > 10^2$) with no obvious asymptotic behaviour. On the other hand, the global scalings (5.7) fall much closer to the actual values for the range $10^2 < Re < 10^4$ and approach an asymptote for $Re > 10^2$. The deviations observed for the highest Re cases have probably a numerical origin: the averaging timespan used to estimate the dissipation rates are likely too short in the most demanding cases to perfectly average out all the fluctuations.

The total thermal and viscous dissipation rates in our spherical shell simulations are thus better described by the sum of two power laws that follow the GL theory than by the sum of the asymptotic laws derived from the individual contributions, which suffers from an unclear separation of the boundary layer and bulk dynamics.

This result also sheds a new light on the placement of our numerical simulations in the GL regime diagram (Fig. 16). Equation (5.7) directly provides the estimated relative contributions of the bulk and boundary layers to the viscous and thermal dissipation rates. Figure 21 shows these different contributions for the numerical models of Table 1 and reveals a completely different balance than in Fig. 16. At low Rayleigh numbers, the estimated boundary layer contributions now dominate both the viscous and thermal dissipation rates. The viscous dissipation rate in the fluid bulk gradually increases with Ra and dominates beyond $Ra > 10^7$. The bulk contribution to the thermal dissipation rate exhibits a similar trend, gradually increasing from roughly 5% at $Ra = 10^4$ to more than 40% at $Ra = 10^9$. While the thermal dissipation rate in the fluid bulk never dominates in the regime explored here, our scaling predict that it will do so for $Ra \gtrsim 3 \times 10^9$. These values would then locate the numerical models with $Ra \leq 10^7$ in the GL regime I of the $Ra - Pr$ parameter space. The cases with $10^7 < Ra < 3 \times 10^9$ would then belong to regime II. The transition to regime IV where the bulk contributions dominate the dissipation rates would then happen around $Ra \simeq 3 \times 10^9$.

While it is not clear that the contributions inferred from the total dissipation rates actually reflect the exact bulk and boundary layer contributions to ϵ_U and ϵ_T, this separation nevertheless allows us to reconcile the classification of our spherical shell convection models in the $Ra - Pr$ parameter space with the prediction of the GL theory for a fluid with $Pr = 1$. Future work that will better characterise and separate the bulk and boundary layer dynamics might help to reconcile the individual scalings (Fig. 16) with the global ones (Fig. 21), especially at low Ra.

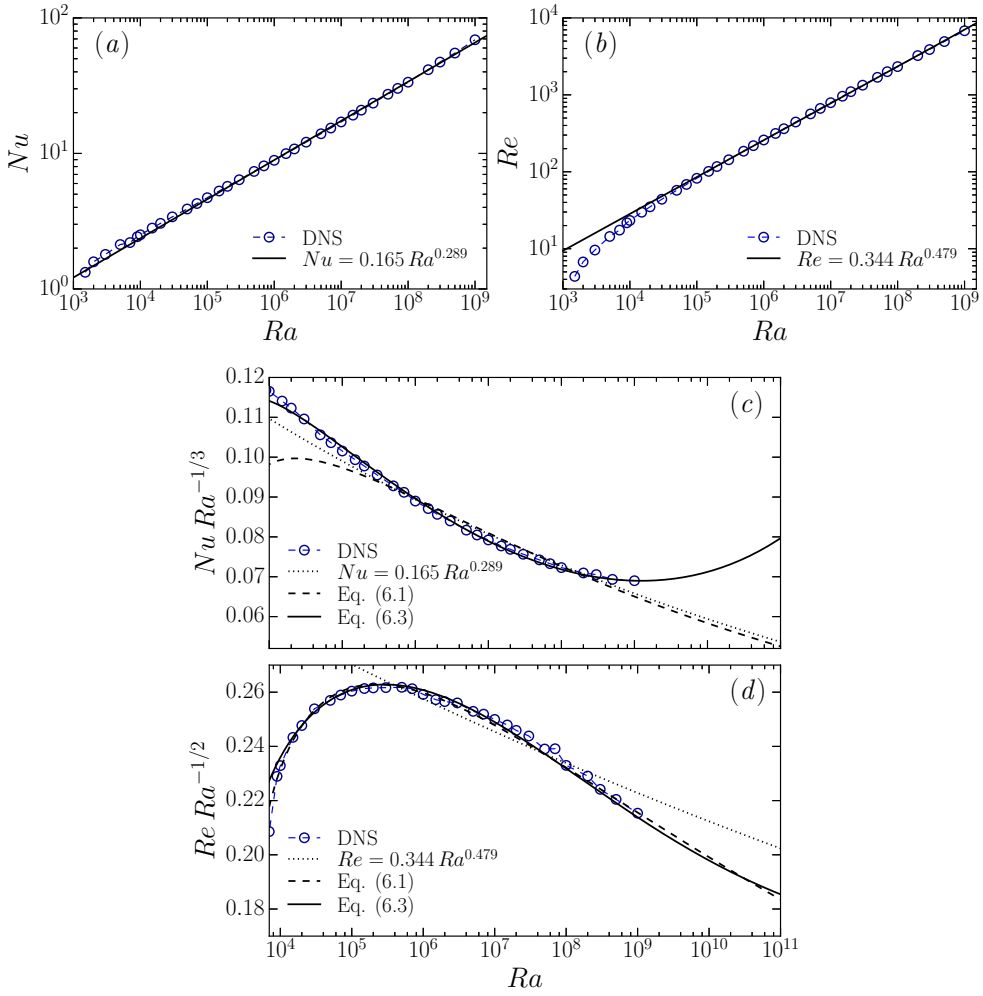

FIGURE 22. (a) Nusselt number versus Rayleigh number. (b) Reynolds number versus Rayleigh number. (c) Compensated Nusselt number versus Rayleigh number. (d) Compensated Reynolds number versus Rayleigh number. The power laws given in panels (a-b) have been derived from a best fit to the cases of Table 1 with $Ra \geq 10^5$. In panels (c-d), the dashed lines correspond to the numerical solution of Eq. (6.1) and the solid lines to the numerical solution of Eq. (6.3).

6. Nusselt and Reynolds numbers scalings

Figure 22 shows Nu and Re as a function of Ra for the cases of Table 1. A simple best fit to the data for the cases with $Ra \geq 10^5$ yields $Nu \sim Ra^{0.289}$ and $Re \sim Ra^{0.479}$, relatively close to $Nu \sim Ra^{2/7}$ and $Re \sim Ra^{1/2}$. While reducing the scaling behaviours of Nu and Re to such simple power laws is a common practice in studies of convection in spherical shells with infinite Prandtl number (e.g. Wolstencroft *et al.* 2009; Deschamps *et al.* 2010), this description might be too simplistic to account for the complex dependence of Nu and Re upon Ra. To illustrate this issue, the panels (c) and (d) of Fig. 22 show the compensated scalings of Nu and Re. The power laws fail to capture the complex behaviour of $Nu(Ra)$ and $Re(Ra)$ and show an increasing deviation from the data

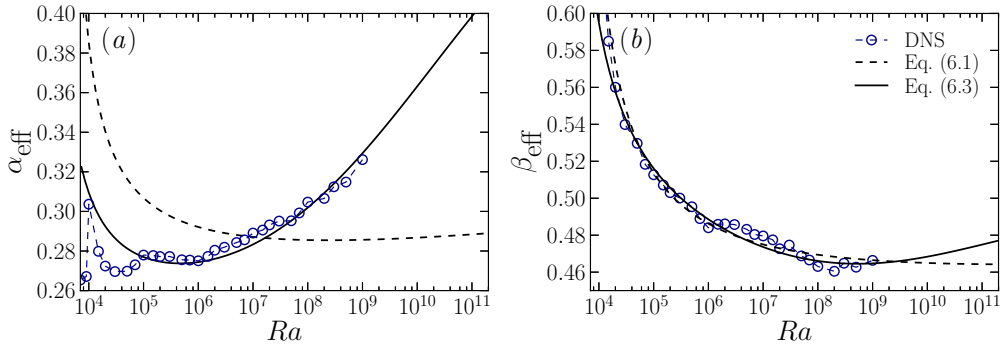

FIGURE 23. (a) $\alpha_{\rm eff}$ versus Ra. (b) $\beta_{\rm eff}$ versus Ra. The dashed black line correspond to the solution of Eq. (6.1), while the solid black line correspond to the solution of Eq. (6.3).

at high Ra. For instance, the 0.289 scaling exponent obtained for the Nusselt number is too steep for $Ra \leq 10^7$ and too shallow for higher Rayleigh numbers.

The GL theory predicts a gradual change of the slopes of $Nu(Ra)$ and $Re(Ra)$ since the flows cross different dynamical regimes when Ra increases. Using the asymptotic laws obtained for the different contributions to the dissipation rates (Eq. 5.8) and the dissipation relations (Eq. 2.9) and (Eq. 2.10), we can derive the following equations that relate Nu and Re to Ra:

$$\begin{aligned} \epsilon_U = \frac{3}{1+\eta+\eta^2}\frac{Ra}{Pr^2}(Nu-1) \quad &= 1.713\, Re^{2.79} + 2.147\, Re^{2.52}\,, \\ \epsilon_T = \frac{3\eta}{1+\eta+\eta^2} Nu \quad &= 0.037\, Re^{0.7} + 0.267\, Re^{0.57}\,. \end{aligned} \tag{6.1}$$

This system of equations can be numerically integrated to derive the scaling laws for Nu and Re. Figure 22(c-d) illustrates the comparison between these integrated values and the actual data, while Fig. 23 shows the local effective exponents $\alpha_{\rm eff}$ and $\beta_{\rm eff}$ of the $Nu(Ra)$ and $Re(Ra)$ laws as a function of Ra:

$$\alpha_{\rm eff} = \frac{\partial \ln Nu}{\partial \ln Ra}; \quad \beta_{\rm eff} = \frac{\partial \ln Re}{\partial \ln Ra}\,. \tag{6.2}$$

While $Re(Ra)$ is nicely described by the solution of Eq. (6.1), some persistent deviations in the $Nu(Ra)$ scaling are noticeable. In particular, $\alpha_{\rm eff}(Ra)$ increases much faster than expected from the scaling law (dashed lines): $\alpha_{\rm eff}(10^9) \simeq 0.325$ while the predicted slope remains close to 0.285. The difficulties to accurately separate the bulk and boundary layer dynamics when deriving the scaling laws for the different contributions to the dissipation rates are once again likely responsible of this misfit.

As demonstrated in the previous section, replacing the sum of the individual dissipation contributions by the global scalings provides a much better fit to ϵ_U and ϵ_T (Fig. 20). We can thus construct another set of equations based on the scaling laws for the total dissipation rates (Eq. 5.7):

$$\begin{aligned} \epsilon_U = \frac{3}{1+\eta+\eta^2}\frac{Ra}{Pr^2}(Nu-1) \quad &= 0.251\, Re^{3} + 7.038\, Re^{5/2}\,, \\ \epsilon_T = \frac{3\eta}{1+\eta+\eta^2} Nu \quad &= 0.004\, Re + 0.446\, Re^{1/2}\,. \end{aligned} \tag{6.3}$$

This system of equation is once again numerically integrated to derive the scaling laws for $Nu(Ra)$ and $Re(Ra)$. The solid black lines displayed in Fig. 22(c-d) and Fig. 23 show

that these scaling laws fall now much closer to the data. They accurately reproduce both $Nu(Ra)$ and $Re(Ra)$ for the whole range of Rayleigh numbers and the gradual change in the slopes $\alpha_{\rm eff}$ and $\beta_{\rm eff}$ are also correctly captured. The improvement of the fit to the data when using (Eq. 6.3) instead of (Eq. 6.1) is the direct consequence of the better description of the total dissipation rates by the global scalings (Eq. 5.7) rather than by the sum of the individual scalings (Eq. 5.8).

Figures 22(*c-d*) and 23 also show an extrapolation of the scaling laws, solution of Eq. (6.3), up to $Ra = 10^{11}$. Interestingly, the scaling laws predict that $\alpha_{\rm eff}$ would become steeper than 1/3 for $Ra \gtrsim 3 - 5 \times 10^9$. This possible transition point to an enhanced heat transport efficiency would then occur at much lower Ra than in RB convection in cartesian or cylindrical cells. For instance, the experiments by Roche *et al.* (2010) showed an enhanced scaling of $Nu \sim Ra^{0.38}$ for $Ra > 7 \times 10^{11}$. Future RB models in spherical shells that will possibly reach $Ra \simeq 10^{10}$ could certainly help to confirm this trend.

7. Conclusion and outlooks

We have studied Rayleigh-Bénard (RB) convection in spherical shells for Rayleigh numbers up to 10^9 and Prandtl number unity. Because of both curvature and radial variations of buoyancy, convection in spherical shells exhibits asymmetric boundary layers. To better characterise this asymmetry, we have conducted a systematic parameter study, varying both the radius ratio and the radial distribution of gravity. Two theories were developed in the past to determine this boundary layer asymmetry. The first one by Jarvis (1993) and Vangelov & Jarvis (1994) hypothesises that both boundary layers adjust their thickness to maintain the same critical boundary layer Rayleigh number; while the second one by Wu & Libchaber (1991) assumes that the thermal fluctuations at mid-depth are statistically symmetrically distributed. Both theories however yield scaling laws in poor agreement with our numerical simulations. On the contrary, we found that the average plume density, or equivalently the average inter-plume spacing, is nearly identical for both boundary layers. An estimation of the average plume density at both spherical bounding surfaces has allowed us to accurately predict the boundary layer asymmetry and the mean bulk temperature for the wide range of spherical shell configurations explored here ($\eta = r_i/r_o$ spanning the range $0.2 \leq \eta \leq 0.95$ and gravity profiles $g \in [r/r_o, 1, (r_o/r)^2, (r_o/r)^5]$).

Because of the lack of experiments and numerical models of non-rotating convection in spherical shells at finite Prandtl numbers, the scaling properties of the Nusselt and the Reynolds numbers are poorly characterised in this geometry. To further address this question, we have conducted numerical models in spherical shells with $\eta = 0.6$ up to $Ra = 10^9$. We have adopted a gravity profile of the form $g = (r_o/r)^2$, which has allowed us to conduct a full dissipation analysis. One of the aims of this study was to check the applicability of the scaling theory by Grossmann & Lohse (2000, 2004) (GL) to convection in spherical shells. One of the prerequisites of this theory is the assumption of Prandtl-Blasius-type (PB) boundary layers. We have thus studied the temperature and horizontal velocity boundary layer profiles. In agreement with the previous findings by Zhou & Xia (2010*a*), the boundary layer profiles have been found to be in fair agreement with the PB profiles, provided the numerical simulations are analysed in a dynamical frame that incorporates the time and spatial variations of the boundary layers. Following the GL central idea, we have then decomposed the viscous and thermal dissipation rates into contributions coming from the fluid bulk and from the boundary layer regions. The detailed analysis of the individual contributions to the viscous and thermal dissipation rates reveals some noticeable discrepancies to the GL theory ($\epsilon_U^{bu} \sim Re^{2.79}$, $\epsilon_U^{bl} \sim Re^{2.52}$,

$\epsilon_T^{bu} \sim Re^{0.7}$ and $\epsilon_T^{bl} \sim Re^{0.57}$). The total dissipation rates, however, can nevertheless be nicely described by the sum of bulk and boundary layer contributions that follow the predicted GL exponents ($\epsilon_U \sim a\,Re^3 + b\,Re^{5/2}$ and $\epsilon_T \sim a\,Re + b\,Re^{1/2}$). This strongly suggests that the inaccurate separation of the boundary layer and bulk dynamics is the reason for the inferior fitting of the individual contributions. These scaling laws have finally been employed to study the scaling properties of the Nusselt and the Reynolds numbers and provide laws that accurately fit the data. Although these laws exhibit a similar behaviour than experiments and numerical simulations of RB convection in cartesian or cylindrical coordinates; some distinction to classical RB cells have also been reported. Our scaling laws predict a continuous increase of the local effective slope of $Nu(Ra)$ from 0.28 at $Ra = 10^6$ to 0.33 at $Ra = 10^9$ and suggest a possible enhanced heat transfer scaling with an effective exponent steeper than 1/3 for $Ra > 5 \times 10^9$. Similar transitions have been observed in some experiments, though at significantly higher Rayleigh numbers ($Ra \sim 10^{11} - 10^{12}$, see Roche *et al.* 2010).

To explore whether the spherical shell geometry is responsible for this difference, additional numerical simulations at higher Rayleigh numbers are required. Ongoing improvements of pseudo-spectral codes for modelling convection in three dimensional spherical shells might help to reach spatial resolutions of the order ($N_r \times \ell_{max} = 2048 \times 2048$) in the coming years (e.g. Schaeffer 2013). Assuming that the minimum admissible mesh size h has to be smaller than the global Kolmogorov scale (Grötzbach 1983; Shishkina *et al.* 2010) yields

$$h \leq \eta_K = \frac{\nu^{3/4}}{\epsilon_U^{1/4}} = \left(\frac{1+\eta+\eta^2}{3}\right)^{1/4} \frac{Pr^{1/2}}{Ra^{1/4}\,(Nu-1)^{1/4}}\,.$$

An extrapolation of the spatial resolutions employed in this study (Table 1) then implies that typical resolutions ($N_r \times \ell_{max} = 2048 \times 2048$) might be sufficient to reach $Ra \simeq 10^{10}$ for the configuration we considered here ($\eta = 0.6$, $g = (r_o/r)^2$). This additional decade in Ra might already be sufficient to ascertain the derived asymptotic scalings.

We thank Andreas Tilgner for fruitful discussions. All the computations have been carried out on the GWDG computer facilities in Göttingen and on the IBM iDataPlex HPC System Hydra at the MPG Rechenzentrum Garching. TG is supported by the Special Priority Program 1488 (PlanetMag, www.planetmag.de) of the German Science Foundation.

Appendix A. Table of results for the numerical models with different geometry and gravity profiles

η	Ra	Nu	Re	λ_T^i/λ_T^o	λ_U^i/λ_U^o	$\epsilon_T^{bu}(\%)$	$\epsilon_U^{bu}(\%)$	$N_r \times \ell_{max}$
				$g = r/r_o$				
0.2	1×10^8	8.27	723.1	0.024/0.023	0.015/0.021	0.27	0.73	97×170
0.2	3×10^8	11.23	1252.4	0.017/0.018	0.012/0.017	0.29	0.76	129×341
0.25	2×10^7	6.92	407.8	0.035/0.034	0.022/0.026	0.27	0.72	65×128
0.3	3×10^6	5.18	188.1	0.054/0.054	0.030/0.035	0.24	0.69	65×128
0.3	5×10^6	5.87	242.1	0.048/0.048	0.027/0.031	0.26	0.71	65×128
0.3	7×10^6	6.40	287.2	0.044/0.045	0.025/0.030	0.26	0.72	73×133

0.3	3×10^7	9.38	595.5	0.029/0.032	0.019/0.023	0.28	0.76	73×133
0.3	3×10^8	18.08	1824.8	0.015/0.017	0.011/0.015	0.29	0.81	97×341
0.35	5×10^6	6.74	274.1	0.047/0.048	0.027/0.031	0.26	0.74	65×128
0.35	3×10^8	21.23	2016.0	0.015/0.016	0.011/0.014	0.30	0.82	129×341
0.4	1×10^6	5.17	139.7	0.067/0.071	0.036/0.041	0.23	0.68	65×128
0.4	3×10^6	6.72	235.3	0.052/0.055	0.029/0.033	0.23	0.75	65×128
0.4	5×10^6	7.65	302.4	0.045/0.048	0.026/0.030	0.26	0.76	73×133
0.45	2×10^6	6.71	215.6	0.056/0.059	0.032/0.036	0.24	0.73	65×128
0.5	1×10^6	6.01	162.4	0.066/0.070	0.037/0.040	0.23	0.72	65×128
0.5	2×10^6	7.22	229.4	0.055/0.058	0.032/0.036	0.24	0.75	65×128
0.5	5×10^6	9.24	359.9	0.043/0.045	0.027/0.029	0.25	0.78	81×133
0.55	2×10^6	7.71	240.2	0.054/0.057	0.031/0.033	0.24	0.76	65×128
0.6	1×10^6	6.80	179.2	0.065/0.067	0.036/0.038	0.22	0.74	65×128
0.6	5×10^6	10.55	392.3	0.042/0.043	0.026/0.027	0.24	0.80	81×133
0.6	5×10^6	10.56	392.2	0.042/0.043	0.026/0.027	0.24	0.80	81×133
0.65	1×10^6	7.11	186.6	0.064/0.066	0.035/0.037	0.23	0.76	73×170
0.7	7×10^5	6.72	162.0	0.070/0.072	0.037/0.039	0.21	0.74	73×170
0.7	1×10^6	7.41	193.1	0.063/0.065	0.035/0.036	0.23	0.76	73×170
0.75	1×10^6	7.64	198.9	0.063/0.064	0.034/0.036	0.22	0.76	97×213
0.8	3×10^6	10.60	347.8	0.046/0.047	0.028/0.028	0.23	0.80	97×426
0.8	4×10^7	22.16	1198.3	0.022/0.022	0.016/0.016	0.26	0.85	129×1024
0.85	7×10^5	7.26	175.5	0.068/0.069	0.037/0.038	0.20	0.76	97×341
0.9	5×10^5	6.73	151.4	0.074/0.075	0.040/0.040	0.22	0.74	97×426
				$g = 1$				
0.2	1×10^8	11.95	1082.7	0.016/0.025	0.011/0.021	0.29	0.78	97×170
0.25	2×10^7	9.35	572.0	0.025/0.036	0.016/0.027	0.25	0.78	81×133
0.3	7×10^6	8.15	377.8	0.033/0.046	0.020/0.031	0.26	0.78	73×133
0.35	6×10^6	8.79	383.9	0.035/0.046	0.021/0.030	0.26	0.79	73×133
0.4	3×10^6	7.98	288.7	0.042/0.054	0.025/0.032	0.24	0.79	65×128
0.4	5×10^6	9.19	371.4	0.036/0.047	0.022/0.029	0.27	0.80	65×128
0.45	5×10^6	9.95	395.4	0.036/0.046	0.022/0.029	0.27	0.80	73×128
0.5	5×10^6	10.57	421.7	0.036/0.045	0.023/0.029	0.26	0.80	81×133
0.55	5×10^6	11.09	434.8	0.037/0.044	0.023/0.028	0.26	0.81	81×133
0.6	3×10^6	10.04	343.3	0.042/0.049	0.026/0.030	0.24	0.80	81×133
0.6	5×10^6	11.68	442.7	0.036/0.042	0.023/0.027	0.26	0.81	81×133
0.65	3×10^6	10.48	355.3	0.042/0.048	0.026/0.029	0.24	0.80	81×133
0.7	1×10^6	7.85	210.0	0.058/0.064	0.033/0.036	0.22	0.77	73×213
0.75	3×10^6	10.82	363.0	0.043/0.047	0.026/0.029	0.24	0.80	97×341
0.8	3×10^6	10.98	367.4	0.043/0.046	0.027/0.028	0.24	0.80	97×426
0.85	1×10^6	8.22	217.5	0.059/0.062	0.033/0.035	0.21	0.76	97×426
0.9	5×10^5	6.83	155.2	0.072/0.074	0.039/0.040	0.21	0.74	97×426
				$g = (r_o/r)^2$				
0.2	5×10^5	5.85	171.9	0.031/0.089	0.017/0.047	0.25	0.80	49×85
0.2	7×10^5	6.45	206.2	0.028/0.082	0.016/0.046	0.24	0.80	49×85
0.2	1×10^6	7.17	248.8	0.026/0.076	0.014/0.044	0.24	0.80	61×106
0.2	1.5×10^6	8.03	308.1	0.022/0.068	0.012/0.041	0.28	0.81	81×170
0.2	2×10^6	8.78	351.9	0.020/0.064	0.011/0.039	0.26	0.82	81×170
0.2	1×10^7	14.19	794.2	0.013/0.040	0.008/0.027	0.30	0.84	97×256

0.2	3×10^7	20.25	1369.5	0.009/0.029	0.006/0.021	0.31	0.84	97×341
0.25	5×10^5	6.29	180.2	0.035/0.087	0.019/0.047	0.26	0.79	49×85
0.3	5×10^5	6.60	185.7	0.038/0.085	0.021/0.046	0.22	0.80	65×128
0.3	1×10^6	8.08	263.2	0.031/0.071	0.017/0.041	0.23	0.81	65×128
0.3	3×10^6	11.11	458.1	0.022/0.053	0.013/0.034	0.29	0.83	73×133
0.3	1×10^7	16.07	803.7	0.015/0.037	0.010/0.025	0.28	0.86	97×256
0.3	5×10^7	25.68	1810.7	0.010/0.024	0.007/0.018	0.30	0.86	161×512
0.35	5×10^5	6.87	187.4	0.041/0.083	0.023/0.045	0.23	0.79	65×128
0.4	5×10^5	7.15	189.0	0.044/0.081	0.024/0.043	0.24	0.78	65×128
0.4	8×10^5	8.07	237.7	0.038/0.072	0.022/0.041	0.22	0.80	65×128
0.4	1×10^6	8.59	266.6	0.036/0.068	0.021/0.039	0.26	0.81	65×128
0.4	3×10^6	11.72	459.1	0.026/0.051	0.016/0.032	0.27	0.83	97×170
0.45	5×10^5	7.26	192.7	0.046/0.080	0.026/0.044	0.24	0.77	65×128
0.45	7×10^5	7.98	226.9	0.042/0.073	0.024/0.041	0.23	0.78	65×128
0.5	5×10^5	7.29	190.6	0.049/0.079	0.028/0.044	0.23	0.76	61×106
0.5	7×10^5	8.01	225.7	0.045/0.072	0.026/0.041	0.23	0.78	65×128
0.5	1×10^6	8.83	270.1	0.041/0.066	0.024/0.039	0.23	0.79	81×170
0.55	5×10^5	7.31	187.3	0.052/0.078	0.029/0.043	0.24	0.78	61×106
0.65	5×10^5	7.36	182.2	0.057/0.076	0.031/0.042	0.21	0.77	61×106
0.7	1.5×10^5	5.22	97.7	0.083/0.106	0.042/0.053	0.19	0.72	73×170
0.7	3×10^5	6.35	138.2	0.068/0.087	0.036/0.046	0.20	0.75	73×170
0.7	5×10^5	7.32	178.3	0.059/0.075	0.032/0.041	0.21	0.76	81×266
0.7	1×10^6	8.83	251.0	0.049/0.063	0.029/0.036	0.22	0.79	73×213
0.75	5×10^5	7.26	174.9	0.062/0.075	0.033/0.041	0.22	0.75	81×266
0.8	5×10^5	7.20	171.2	0.064/0.074	0.035/0.040	0.20	0.75	81×266
0.8	1×10^6	8.71	240.8	0.053/0.062	0.030/0.035	0.22	0.78	97×341
0.8	3×10^6	11.81	409.2	0.039/0.046	0.024/0.028	0.23	0.81	97×426
0.85	1×10^6	8.62	235.5	0.055/0.061	0.031/0.034	0.22	0.78	97×426
0.9	1×10^5	4.47	72.2	0.108/0.116	0.053/0.056	0.17	0.68	97×266
0.9	5×10^5	7.04	163.8	0.069/0.074	0.037/0.040	0.21	0.75	97×426
0.9	1×10^6	8.54	230.2	0.057/0.061	0.032/0.034	0.22	0.78	97×512
0.95	1×10^5	4.41	70.4	0.112/0.116	0.054/0.056	0.17	0.68	97×512
				$g = (r_o/r)^5$				
0.2	3×10^4	9.15	206.2	0.017/0.117	0.009/0.055	0.24	0.85	65×128
0.2	5×10^4	10.59	265.7	0.015/0.100	0.007/0.048	0.23	0.85	65×128
0.2	7×10^4	11.90	313.9	0.013/0.089	0.007/0.043	0.28	0.85	65×133
0.25	6×10^4	9.52	238.3	0.020/0.105	0.011/0.055	0.26	0.82	65×128
0.3	7×10^4	8.69	212.7	0.025/0.107	0.013/0.056	0.24	0.83	65×128
0.3	1×10^5	9.77	251.9	0.023/0.095	0.012/0.050	0.23	0.83	65×133
0.3	3×10^5	13.94	440.1	0.015/0.070	0.009/0.040	0.24	0.84	65×133
0.3	3×10^6	27.99	1327.6	0.008/0.035	0.005/0.023	0.29	0.86	161×426
0.35	2×10^5	10.75	307.3	0.023/0.083	0.013/0.045	0.23	0.83	65×133
0.4	1×10^5	7.94	189.5	0.034/0.104	0.018/0.055	0.23	0.80	65×133
0.4	3×10^5	11.08	327.1	0.024/0.076	0.014/0.043	0.23	0.83	65×133
0.4	5×10^5	13.04	422.0	0.020/0.067	0.012/0.039	0.27	0.83	65×133
0.45	3×10^5	10.25	290.0	0.029/0.077	0.016/0.042	0.26	0.81	65×133
0.5	1×10^5	6.95	153.4	0.046/0.106	0.025/0.053	0.22	0.76	65×133
0.5	3×10^5	9.53	265.8	0.033/0.079	0.019/0.044	0.23	0.80	65×133
0.55	3×10^5	8.88	239.3	0.038/0.081	0.022/0.045	0.25	0.78	65×133

0.6	3×10^5	8.41	216.6	0.043/0.081	0.024/0.044	0.23	0.78	65×133
0.6	5×10^5	9.69	278.4	0.037/0.071	0.021/0.040	0.24	0.80	73×170
0.6	7×10^5	10.69	329.1	0.033/0.065	0.020/0.038	0.24	0.81	73×170
0.6	1×10^7	23.28	1199.9	0.015/0.031	0.011/0.022	0.28	0.84	129×341
0.65	3×10^5	7.97	199.8	0.047/0.082	0.026/0.044	0.24	0.77	65×170
0.7	3×10^5	7.60	183.9	0.052/0.082	0.029/0.044	0.22	0.77	65×170
0.7	5×10^5	8.76	236.1	0.045/0.072	0.026/0.040	0.22	0.78	65×170
0.7	7×10^5	9.66	279.4	0.041/0.066	0.024/0.038	0.22	0.78	65×170
0.75	5×10^5	8.34	218.8	0.050/0.072	0.028/0.040	0.21	0.78	65×256
0.8	7×10^5	8.80	240.0	0.049/0.066	0.028/0.038	0.22	0.79	65×256
0.8	7×10^5	8.78	239.7	0.049/0.066	0.028/0.037	0.23	0.78	97×426
0.85	7×10^5	8.41	223.2	0.054/0.066	0.030/0.037	0.22	0.78	97×426
0.9	1×10^6	8.95	248.9	0.052/0.060	0.030/0.034	0.21	0.78	97×512

Table 2: Summary table of $Pr = 1$ numerical simulations with various radius ratio η and gravity profiles $g(r)$.

REFERENCES

Ahlers, G., Brown, E., Fontenele Araujo, F., Funfschilling, D., Grossmann, S. & Lohse, D. 2006 Non-Oberbeck Boussinesq effects in strongly turbulent Rayleigh Bénard convection. *Journal of Fluid Mechanics* **569**, 409–445.

Ahlers, G., Grossmann, S. & Lohse, D. 2009 Heat transfer and large scale dynamics in turbulent Rayleigh-Bénard convection. *Reviews of Modern Physics* **81**, 503–537.

Amati, G., Koal, K., Massaioli, F., Sreenivasan, K. R. & Verzicco, R. 2005 Turbulent thermal convection at high Rayleigh numbers for a Boussinesq fluid of constant Prandtl number. *Physics of Fluids* **17** (12), 121701.

Bailon-Cuba, J., Emran, M. S. & Schumacher, J. 2010 Aspect ratio dependence of heat transfer and large-scale flow in turbulent convection. *Journal of Fluid Mechanics* **655**, 152–173.

Bercovici, D., Schubert, G. & Glatzmaier, G. A. 1992 Three-dimensional convection of an infinite-Prandtl-number compressible fluid in a basally heated spherical shell. *Journal of Fluid Mechanics* **239**, 683–719.

Bercovici, D., Schubert, G., Glatzmaier, G. A. & Zebib, A. 1989 Three-dimensional thermal convection in a spherical shell. *Journal of Fluid Mechanics* **206**, 75–104.

Blasius, H. 1908 Grenzschichten in Flüssigkeiten mit kleiner Reibung. *Z. Math. Phys.* **56**, 1–37.

Breuer, M., Wessling, S., Schmalzl, J. & Hansen, U. 2004 Effect of inertia in Rayleigh-Bénard convection. *Phys. Rev. E* **69** (2), 026302.

Calzavarini, E., Lohse, D., Toschi, F. & Tripiccione, R. 2005 Rayleigh and Prandtl number scaling in the bulk of Rayleigh-Bénard turbulence. *Physics of Fluids* **17** (5), 055107.

Castaing, B., Gunaratne, G., Kadanoff, L., Libchaber, A. & Heslot, F. 1989 Scaling of hard thermal turbulence in Rayleigh-Bénard convection. *Journal of Fluid Mechanics* **204**, 1–30.

Chavanne, X., Chillà, F., Castaing, B., Hébral, B., Chabaud, B. & Chaussy, J. 1997 Observation of the Ultimate Regime in Rayleigh-Bénard Convection. *Physical Review Letters* **79**, 3648–3651.

Cheng, J. S., Stellmach, S., Ribeiro, A., Grannan, A., King, E. M. & Aurnou, J. M. 2015 Laboratory-numerical models of rapidly rotating convection in planetary cores. *Geophysical Journal International* **201**, 1–17.

Chillà, F. & Schumacher, J. 2012 New perspectives in turbulent Rayleigh-Bénard convection. *The European Physical Journal E* **35** (7).

Choblet, G. 2012 On the scaling of heat transfer for mixed heating convection in a spherical shell. *Physics of the Earth and Planetary Interiors* **206**, 31–42.

Christensen, U. & Wicht, J. 2007 *Numerical dynamo simulations*, pp. 97–114.

Christensen, U. R. & Aubert, J. 2006 Scaling properties of convection-driven dynamos in rotating spherical shells and application to planetary magnetic fields. *Geophysical Journal International* **166**, 97–114.

Christensen, U. R., Aubert, J., Cardin, P., Dormy, E., Gibbons, S., Glatzmaier, G. A., Grote, E., Honkura, Y., Jones, C., Kono, M., Matsushima, M., Sakuraba, A., Takahashi, F., Tilgner, A., Wicht, J. & Zhang, K. 2001 A numerical dynamo benchmark. *Physics of the Earth and Planetary Interiors* **128**, 25–34.

Deschamps, F., Tackley, P. J. & Nakagawa, T. 2010 Temperature and heat flux scalings for isoviscous thermal convection in spherical geometry. *Geophysical Journal International* **182**, 137–154.

du Puits, R., Resagk, C. & Thess, A. 2013 Thermal boundary layers in turbulent Rayleigh-Bénard convection at aspect ratios between 1 and 9. *New Journal of Physics* **15** (1), 013040.

Feldman, Y. & Colonius, T. 2013 On a transitional and turbulent natural convection in spherical shells. *International Journal of Heat and Mass Transfer* **64** (0), 514–525.

Feudel, F., Bergemann, K., Tuckerman, L. S., Egbers, C., Futterer, B., Gellert, M. & Hollerbach, R. 2011 Convection patterns in a spherical fluid shell. *Phys. Rev. E* **83** (4), 046304.

Funfschilling, D., Brown, E., Nikolaenko, A. & Ahlers, G. 2005 Heat transport by turbulent Rayleigh Bénard convection in cylindrical samples with aspect ratio one and larger. *Journal of Fluid Mechanics* **536**, 145–154.

Futterer, B., Egbers, C., Dahley, N., Koch, S. & Jehring, L. 2010 First identification of sub- and supercritical convection patterns from 'GeoFlow', the geophysical flow simulation experiment integrated in Fluid Science Laboratory. *Acta Astronautica* **66** (1-2), 193–200.

Futterer, B., Krebs, A., Plesa, A.-C., F., Zaussinger, R., Hollerbach, D., Breuer & C., Egbers 2013 Sheet-like and plume-like thermal flow in a spherical convection experiment performed under microgravity. *Journal of Fluid Mechanics* **735**, 647–683.

Gastine, T. & Wicht, J. 2012 Effects of compressibility on driving zonal flow in gas giants. *Icarus* **219**, 428–442.

Gastine, T., Wicht, J. & Aurnou, J. 2013 Zonal flow regimes in rotating spherical shells: An application to giant planets. *Icarus* **225**, 156–172.

Gilman, P. A. & Glatzmaier, G. A. 1981 Compressible convection in a rotating spherical shell - I - Anelastic equations. *ApJS* **45**, 335–349.

Grossmann, S. & Lohse, D. 2000 Scaling in thermal convection: a unifying theory. *Journal of Fluid Mechanics* **407**, 27–56.

Grossmann, S. & Lohse, D. 2004 Fluctuations in turbulent Rayleigh-Bénard convection: The role of plumes. *Physics of Fluids* **16**, 4462–4472.

Grötzbach, G. 1983 Spatial resolution requirements for direct numerical simulation of the Rayleigh-Bénard convection. *Journal of Computational Physics* **49**, 241–264.

Hart, J. E., Glatzmaier, G. A. & Toomre, J. 1986 Space-laboratory and numerical simulations of thermal convection in a rotating hemispherical shell with radial gravity. *Journal of Fluid Mechanics* **173**, 519–544.

Jarvis, G. T. 1993 Effects of curvature on two-dimensional models of mantle convection - Cylindrical polar coordinates. *J. Geophys. Res.* **98**, 4477–4485.

Jarvis, G. T., Glatzmaier, G. A. & Vangelov, V. I. 1995 Effects of curvature, aspect ratio and plan form in two- and three-dimensional spherical models of thermal convection. *Geophysical and Astrophysical Fluid Dynamics* **79**, 147–171.

Jones, C. A., Boronski, P, Brun, A. S., Glatzmaier, G. A., Gastine, T., Miesch, M. S. & Wicht, J. 2011 Anelastic convection-driven dynamo benchmarks. *Icarus* **216**, 120–135.

Kerr, R. M. & Herring, J. R. 2000 Prandtl number dependence of Nusselt number in direct numerical simulations. *Journal of Fluid Mechanics* **419**, 325–344.

King, E. M., Soderlund, K. M., Christensen, U. R., Wicht, J. & Aurnou, J. M. 2010 Convective heat transfer in planetary dynamo models. *Geochemistry, Geophysics, Geosystems* **11**, 6016.

King, E. M., Stellmach, S. & Aurnou, J. M. 2012 Heat transfer by rapidly rotating Rayleigh-Bénard convection. *Journal of Fluid Mechanics* **691**, 568–582.

King, E. M., Stellmach, S. & Buffett, B. 2013 Scaling behaviour in Rayleigh-Bénard convection with and without rotation. *Journal of Fluid Mechanics* **717**, 449–471.

Lakkaraju, R., Stevens, R. J. A. M., Verzicco, R., Grossmann, S., Prosperetti, A., Sun, C. & Lohse, D. 2012 Spatial distribution of heat flux and fluctuations in turbulent Rayleigh-Bénard convection. *Phys. Rev. E* **86** (5), 056315.

Lam, S., Shang, X.-D., Zhou, S.-Q. & Xia, K.-Q. 2002 Prandtl number dependence of the viscous boundary layer and the Reynolds numbers in Rayleigh-Bénard convection. *Phys. Rev. E* **65** (6), 066306.

Lathrop, D. P., Fineberg, J. & Swinney, H. L. 1992 Turbulent flow between concentric rotating cylinders at large Reynolds number. *Physical Review Letters* **68**, 1515–1518.

Liu, Y. & Ecke, R. E. 2011 Local temperature measurements in turbulent rotating Rayleigh-Bénard convection. *Phys. Rev. E* **84** (1), 016311.

Malkus, W. V. R. 1954 The Heat Transport and Spectrum of Thermal Turbulence. *Royal Society of London Proceedings Series A* **225**, 196–212.

Niemela, J. J., Skrbek, L., Sreenivasan, K. R. & Donnelly, R. J. 2000 Turbulent convection at very high Rayleigh numbers. *Nature* **404**, 837–840.

O'Farrell, K. A., Lowman, J. P. & Bunge, H.-P. 2013 Comparison of spherical-shell and plane-layer mantle convection thermal structure in viscously stratified models with mixed-mode heating: implications for the incorporation of temperature-dependent parameters. *Geophysical Journal International* **192**, 456–472.

Parmentier, E. M. & Sotin, C. 2000 Three-dimensional numerical experiments on thermal convection in a very viscous fluid: Implications for the dynamics of a thermal boundary layer at high Rayleigh number. *Physics of Fluids* **12**, 609–617.

Prandtl, L. 1905 *Verhandlungen des III. Int. Math. Kongr., Heidelberg, 1904*. Leipzig: Teubner, p. 484–491.

Puthenveettil, B. A. & Arakeri, J. H. 2005 Plume structure in high-Rayleigh-number convection. *Journal of Fluid Mechanics* **542**, 217–249.

Roche, P.-E., Gauthier, F., Kaiser, R. & Salort, J. 2010 On the triggering of the Ultimate Regime of convection. *New Journal of Physics* **12** (8), 085014.

Scanlan, J. A., Bishop, E. H. & Powe, R. E. 1970 Natural convection heat transfer between concentric spheres. *International Journal of Heat and Mass Transfer* **13** (12), 1857–1872.

Schaeffer, N. 2013 Efficient spherical harmonic transforms aimed at pseudospectral numerical simulations. *Geochemistry, Geophysics, Geosystems* **14**, 751–758.

Schlichting, H. & Gersten, K. 2000 *Boundary-Layer Theory*. Berlin: Springer-Verlag.

Shahnas, H. M., Lowman, J. P., Jarvis, G. T. & Bunge, H.-P. 2008 Convection in a spherical shell heated by an isothermal core and internal sources: Implications for the thermal state of planetary mantles. *Physics of the Earth and Planetary Interiors* **168**, 6–15.

Shi, N., Emran, M. S. & Schumacher, J. 2012 Boundary layer structure in turbulent Rayleigh-Bénard convection. *Journal of Fluid Mechanics* **706**, 5–33.

Shishkina, O., Stevens, R. J. A. M., Grossmann, S. & Lohse, D. 2010 Boundary layer structure in turbulent thermal convection and its consequences for the required numerical resolution. *New Journal of Physics* **12** (7), 075022.

Shishkina, O. & Thess, A. 2009 Mean temperature profiles in turbulent Rayleigh-Bénard convection of water. *Journal of Fluid Mechanics* **633**, 449.

Shraiman, B. I. & Siggia, E. D. 1990 Heat transport in high-Rayleigh-number convection. *Phys. Rev. A* **42**, 3650–3653.

Siggia, E. D. 1994 High rayleigh number convection. *Annual Review of Fluid Mechanics* **26**, 137–168.

Sotin, C. & Labrosse, S. 1999 Three-dimensional thermal convection in an iso-viscous, infinite Prandtl number fluid heated from within and from below: applications to the transfer of heat through planetary mantles. *Physics of the Earth and Planetary Interiors* **112**, 171–190.

Stevens, R. J. A. M., van der Poel, E. P., Grossmann, S. & Lohse, D. 2013 The unifying

theory of scaling in thermal convection: the updated prefactors. *Journal of Fluid Mechanics* **730**, 295–308.

Stevens, R. J. A. M., Verzicco, R. & Lohse, D. 2010 Radial boundary layer structure and Nusselt number in Rayleigh-Bénard convection. *Journal of Fluid Mechanics* **643**, 495–507.

Stevens, R. J. A. M., Zhou, Q., Grossmann, S., Verzicco, R., Xia, K.-Q. & Lohse, D. 2012 Thermal boundary layer profiles in turbulent Rayleigh-Bénard convection in a cylindrical sample. *Phys. Rev. E* **85** (2), 027301.

Sun, C., Cheung, Y.-H. & Xia, K.-Q. 2008 Experimental studies of the viscous boundary layer properties in turbulent Rayleigh-Bénard convection. *Journal of Fluid Mechanics* **605**, 79–113.

Tilgner, A. 1996 High-Rayleigh-number convection in spherical shells. *Phys. Rev. E* **53**, 4847–4851.

Tilgner, A. & Busse, F. H. 1997 Finite-amplitude convection in rotating spherical fluid shells. *Journal of Fluid Mechanics* **332**, 359–376.

Vangelov, V. I. & Jarvis, G. T. 1994 Geometrical effects of curvature in axisymmetric spherical models of mantle convection. *J. Geophys. Res.* **99**, 9345–9358.

Verzicco, R. 2003 Turbulent thermal convection in a closed domain: viscous boundary layer and mean flow effects. *European Physical Journal B* **35**, 133–141.

Verzicco, R. & Camussi, R. 1999 Prandtl number effects in convective turbulence. *Journal of Fluid Mechanics* **383**, 55–73.

Wicht, J. 2002 Inner-core conductivity in numerical dynamo simulations. *Physics of the Earth and Planetary Interiors* **132**, 281–302.

Wolstencroft, M., Davies, J. H. & Davies, D. R. 2009 Nusselt-Rayleigh number scaling for spherical shell Earth mantle simulation up to a Rayleigh number of 10^9. *Physics of the Earth and Planetary Interiors* **176**, 132–141.

Wu, X.-Z. & Libchaber, A. 1991 Non-Boussinesq effects in free thermal convection. *Phys. Rev. A* **43**, 2833–2839.

Xu, X., Bajaj, K. M. S. & Ahlers, G. 2000 Heat Transport in Turbulent Rayleigh-Bénard Convection. *Physical Review Letters* **84**, 4357.

Zebib, A., Schubert, G. & Straus, J. M. 1980 Infinite Prandtl number thermal convection in a spherical shell. *Journal of Fluid Mechanics* **97**, 257–277.

Zhang, J., Childress, S. & Libchaber, A. 1997 Non-Boussinesq effect: Thermal convection with broken symmetry. *Physics of Fluids* **9**, 1034–1042.

Zhou, Q., Stevens, R. J. A. M., Sugiyama, K., Grossmann, S., Lohse, D. & Xia, K.-Q. 2010 Prandtl-Blasius temperature and velocity boundary-layer profiles in turbulent Rayleigh-Bénard convection. *Journal of Fluid Mechanics* **664**, 297–312.

Zhou, Q. & Xia, K.-Q. 2010*a* Measured Instantaneous Viscous Boundary Layer in Turbulent Rayleigh-Bénard Convection. *Physical Review Letters* **104** (10), 104301.

Zhou, Q. & Xia, K.-Q. 2010*b* Physical and geometrical properties of thermal plumes in turbulent Rayleigh-Bénard convection. *New Journal of Physics* **12** (7), 075006.